

CLASH: A CENSUS OF MAGNIFIED STAR-FORMING GALAXIES AT $z \sim 6 - 8$ *

L.D. BRADLEY¹, A. ZITRIN^{2,27}, D. COE¹, R. BOUWENS³, M. POSTMAN¹, I. BALESTRA^{4,5}, C. GRILLO⁶, A. MONNA^{7,8}, P. ROSATI⁹, S. SEITZ^{7,8}, O. HOST⁶, D. LEMZE¹⁰, J. MOUSTAKAS¹¹, L.A. MOUSTAKAS¹², X. SHU¹³, W. ZHENG¹⁰, T. BROADHURST^{14,15}, M. CARRASCO^{2,16}, S. JOUVEL^{17,18}, A. KOEKEMOER¹, E. MEDEZINSKI¹⁰, M. MENEGHETTI^{12,19,20}, M. NONINO⁴, R. SMIT³, K. UMETSU²¹, M. BARTELMANN², N. BENÍTEZ²², M. DONAHUE²³, H. FORD¹⁰, L. INFANTE¹⁶, Y. JIMENEZ-TEJA²², D. KELSON²⁴, O. LAHAV¹⁸, D. MAOZ²⁵, P. MELCHIOR²⁶, J. MERTEN¹², AND A. MOLINO²²

Astrophysical Journal, Accepted 2014 June 17

ABSTRACT

We utilize 16 band *Hubble Space Telescope* (*HST*) observations of 18 lensing clusters obtained as part of the Cluster Lensing And Supernova survey with Hubble (CLASH) Multi-Cycle Treasury program to search for $z \sim 6 - 8$ galaxies. We report the discovery of 204, 45, and 13 Lyman-break galaxy candidates at $z \sim 6$, $z \sim 7$, and $z \sim 8$, respectively, identified from purely photometric redshift selections. This large sample, representing nearly an order of magnitude increase in the number of magnified star-forming galaxies at $z \sim 6 - 8$ presented to date, is unique in that we have observations in four WFC3/UVIS UV, seven ACS/WFC optical, and all five WFC3/IR broadband filters, which enable very accurate photometric redshift selections. We construct detailed lensing models for 17 of the 18 clusters to estimate object magnifications and to identify two new multiply lensed $z \gtrsim 6$ candidates. The median magnifications over the 17 clusters are 4, 4, and 5 for the $z \sim 6$, $z \sim 7$, and $z \sim 8$ samples, respectively, over an average area of 4.5 arcmin² per cluster. We compare our observed number counts with expectations based on convolving “blank” field UV luminosity functions through our cluster lens models and find rough agreement down to ~ 27 mag, where we begin to suffer significant incompleteness. In all three redshift bins, we find a higher number density at brighter observed magnitudes than the field predictions, empirically demonstrating for the first time the enhanced efficiency of lensing clusters over field surveys. Our number counts also are in general agreement with the lensed expectations from the cluster models, especially at $z \sim 6$, where we have the best statistics.

Subject headings: galaxies: evolution — galaxies: high-redshift — gravitational lensing: strong

* Based on observations made with the NASA/ESA *Hubble Space Telescope*, obtained at the Space Telescope Science Institute, which is operated by the Association of Universities for Research in Astronomy under NASA contract NAS5-26555. These observations are associated with programs 12065-12069, 12100-12104, and 12451-12460.

¹ Space Telescope Science Institute, 3700 San Martin Drive, Baltimore, MD 21218, USA

² Institut für Theoretische Astrophysik, Zentrum für Astronomie, Institut für Theoretische Astrophysik, Albert-Ueberle-Str. 2, D-29120 Heidelberg, Germany

³ Leiden Observatory, Leiden University, Leiden, The Netherlands

⁴ INAF/Osservatorio Astronomico di Trieste, via G.B. Tiepolo 11, I-34143 Trieste, Italy

⁵ INAF/Osservatorio Astronomico di Capodimonte, via Moiariello 16, I-80131 Napoli, Italy

⁶ Dark Cosmology Centre, Niels Bohr Institute, University of Copenhagen, Juliane Mariesvej 30, DK-2100 Copenhagen, Denmark

⁷ University Observatory Munich, Scheinerstrasse 1, D-81679 Munich, Germany

⁸ Max Planck Institute for Extraterrestrial Physics, Giessenbachstrasse, D-85748 Garching, Germany

⁹ ESO-European Southern Observatory, D-85748 Garching bei München, Germany

¹⁰ Department of Physics and Astronomy, The Johns Hopkins University, Baltimore, MD 21218, USA

¹¹ Department of Physics & Astronomy, Siena College, 515 Loudon Road, Loudonville, NY 12211, USA

¹² Jet Propulsion Laboratory, California Institute of Technology, Pasadena, CA 91109, USA

¹³ Department of Astronomy, University of Science and Technology of China, Hefei, Anhui 230026, China

¹⁴ Department of Theoretical Physics and History of Science, University of the Basque Country UPV/EHU, PO Box 644, E-

48080 Bilbao, Spain

¹⁵ Ikerbasque, Basque Foundation for Science, Alameda Urquijo, 36-5 Plaza Bizkaia E-48011, Bilbao, Spain

¹⁶ Centro de Astro-Ingeniería, Departamento de Astronomía y Astrofísica, Pontificia Universidad Católica de Chile, V. Mackenna 4860, Santiago, Chile

¹⁷ Institut de Ciències de l’Espai (IEEC-CSIC), E-08193 Bellaterra (Barcelona), Spain

¹⁸ Department of Physics and Astronomy, University College London, London, WC1E 6BT, UK

¹⁹ INAF/Osservatorio Astronomico di Bologna, via Ranzani 1, I-40127 Bologna, Italy

²⁰ INFN, Sezione di Bologna, Via Ranzani 1, I-40127 Bologna, Italy

²¹ Institute of Astronomy and Astrophysics, Academia Sinica, PO Box 23-141, Taipei 10617, Taiwan

²² Instituto de Astrofísica de Andalucía (IAA-CSIC), E-18008 Granada, Spain

²³ Department of Physics and Astronomy, Michigan State University, East Lansing, MI 48824, USA

²⁴ Observatories of the Carnegie Institution of Washington, Pasadena, CA, USA

²⁵ School of Physics and Astronomy, Tel Aviv University, Tel-Aviv I-69978, Israel

²⁶ Center for Cosmology and Astro-Particle Physics & Department of Physics, The Ohio State University, Columbus, OH 43210, USA

²⁷ Hubble Fellow

1. INTRODUCTION

The improved *Hubble Space Telescope* has revolutionized our ability to study galaxies in the early universe at redshifts $z \gtrsim 6$. The ultra-deep WFC3/IR observations of the Hubble Ultra-Deep Field from the HUDF09 (Bouwens et al. 2011) and HUDF12 (Ellis et al. 2013) campaigns, its two ultra-deep parallel fields, and the deep wide-area WFC3/IR Early Release Science (ERS) observations (Windhorst et al. 2011) have revealed a large sample of ~ 200 $z \sim 7 - 8$ Lyman-break galaxy (LBG) candidates (Bouwens et al. 2011; Lorenzoni et al. 2011; McLure et al. 2011; Schenker et al. 2013; McLure et al. 2013).

Complementary WFC3/IR surveys have further increased the sample of $z \sim 7 - 8$ galaxies, including those obtained as part of the Cosmic Assembly Near-Infrared Deep Extragalactic Legacy Survey (CANDELS; Grogin et al. 2011; Koekemoer et al. 2011; Oesch et al. 2012; Yan et al. 2012) Multi-Cycle Treasury (MCT) program, the Brightest of Reionizing Galaxies (BoRG; Trenti et al. 2011, 2012a; Bradley et al. 2012b) and the Hubble Infrared Pure Parallel Imaging Extragalactic Survey (HIPPIES; Yan et al. 2011). Together, these data sets have allowed for the first detailed studies of galaxies firmly in the reionization epoch at $z \sim 7 - 8$, including their physical properties (e.g., Oesch et al. 2010a; Labbé et al. 2010), rest-frame UV-continuum slopes (e.g., Wilkins et al. 2011; Bouwens et al. 2012b; Dunlop et al. 2013; Bouwens et al. 2013), clustering (Trenti et al. 2012b), nebular line emission (Labbé et al. 2013; Smit et al. 2014), and luminosity function (e.g., Bouwens et al. 2011; Oesch et al. 2012; Bradley et al. 2012b; Schenker et al. 2013; McLure et al. 2013).

Gravitational lensing by massive galaxy clusters has also been highlighted as a powerful tool in the discovery and study of the properties of faint high-redshift galaxies (e.g., Kneib et al. 2004; Egami et al. 2005; Bradley et al. 2008; Richard et al. 2008; Zheng et al. 2009; Bradač et al. 2009; Bouwens et al. 2009; Hall et al. 2012; Bradač et al. 2012; Bradley et al. 2012a; Zitrin et al. 2012b). Of particular note, this includes the recent discoveries of two $z \sim 9$ candidates behind MACSJ1115.9+0129 and MACSJ1720.3+3536 (Bouwens et al. 2012a), a $z \sim 9.6$ candidate behind MACSJ1149.6+2223 (Zheng et al. 2012), and a triply lensed candidate at $z \sim 10.7$ behind MACSJ0647.8+7015 (Coe et al. 2013), all identified by the Cluster Lensing And Supernova survey with Hubble (CLASH; Postman et al. 2012) MCT program.

Massive galaxy clusters can act as gravitational “cosmic telescopes”, considerably magnifying both the apparent luminosity and size of background sources. The flux amplification provides a deeper effective limiting magnitude of the observations, allowing for the identification of high-redshift galaxies that otherwise would have remained undetected. Likewise, the brighter apparent magnitude of magnified high-redshift sources can place them within reach of ground-based spectroscopy, as recently demonstrated by the spectroscopic confirmation of a lensed LBG in Abell 383 at $z = 6.027$ identified by Richard et al. (2011) and A1703-zD6 (Bradley et al. 2012a) at $z = 7.045$ (Schenker et al. 2012), which is the highest-redshift lensed galaxy with a spectroscopic confirmation. Magnification also provides an effective in-

crease in spatial resolution, enabling detailed studies of the sizes and morphologies of high-redshift galaxies that otherwise would not be possible (e.g., Franx et al. 1997; Kneib et al. 2004; Bradley et al. 2008; Zheng et al. 2009; Swinbank et al. 2009; Bradley et al. 2012a; Zitrin et al. 2012b; Zheng et al. 2012; Sharon et al. 2012).

Here we utilize the 16 band *HST* WFC3/UVIS, ACS/WFC, and WFC3/IR observations of 18 lensing clusters obtained as part of the CLASH MCT program to search for $z \sim 6 - 8$ galaxies. This cluster sample includes all five CLASH clusters selected based on their lensing strength (the other 20 were X-ray selected) and four of the six clusters chosen to be part of the Hubble Frontier Fields (HFF) program.²⁹ We identify the high-redshift galaxy candidates from their photometric redshifts, taking advantage of the presence of the Lyman-break feature in their spectral energy distributions (SEDs) (Steidel et al. 1996). Our resulting sample of LBG candidates represents the largest sample of magnified star-forming galaxies at $z \sim 6 - 8$ presented to date. This lensed galaxy sample is unique in that we have observations in seven ACS optical and all five WFC3/IR broadband filters, which enable very accurate photometric redshift selections. Using strong lensing models for 17 of the 18 clusters (RXJ1532 is excluded because of the uncertainty in its strong lensing model; see Section 6), we derive the expected number densities of high-redshift candidates behind these clusters.

This paper is organized as follows. We begin with a description of the observations in Section 2 and discuss our photometry and catalog construction in Section 3. We discuss the photometric redshifts in Section 4 and our high-redshift galaxy sample selection in Section 5. In Section 6, we describe our detailed cluster lens models. In Section 7, we compare the number densities of our high-redshift galaxy sample with those found in “blank” field surveys. Finally, we summarize our results in Section 8. Throughout this paper we adopt a cosmology with $\Omega_m = 0.3$, $\Omega_\Lambda = 0.7$, and $H_0 = 70 \text{ km s}^{-1} \text{ Mpc}^{-1}$. This provides an angular scale of $5.7 \text{ kpc arcsec}^{-1}$, $5.2 \text{ kpc arcsec}^{-1}$, and $4.8 \text{ kpc arcsec}^{-1}$ (proper) at $z = 6.0, 7.0$, and 8.0 , respectively. We refer to the *HST* F814W, F850LP, F105W, F110W, F125W, F140W, and F160W bands as I_{814} , z_{850} , Y_{105} , J_{110} , J_{125} , JH_{140} , and H_{160} , respectively. All magnitudes are expressed in the AB photometric system (Oke 1974).

2. OBSERVATIONS

CLASH is a 524 orbit multi-cycle treasury program to observe 25 galaxy clusters to a total depth of 20 orbits each, incorporating archival *HST* data for our cluster sample whenever possible (Postman et al. 2012). Each cluster is observed using WFC3/UVIS, ACS/WFC, and WFC3/IR to obtain imaging in 16 broadband filters³⁰ spanning from 0.2 to $1.7 \mu\text{m}$ (for the throughput curves of each filter, see Postman et al. 2012 or Jouvel et al. 2014). For this paper, we include the observations of 18

²⁹ For details, see <http://www.stsci.edu/hst/campaigns/frontier-fields/>

³⁰ Some clusters have additional archival data with the ACS F555W filter, which is not a standard filter in our CLASH program. Taking advantage of the archival F555W data, four of our clusters have observations in 17 *HST* bands.

Table 1
Observational Details for the Cluster Sample

Cluster Name	Cluster Alias ^a	α_{J2000} ^b	δ_{J2000} ^b	z_{clus}	$E(B - V)$	Start Date	End Date
Abell 383	A383	02:48:03.36	-03:31:44.7	0.187	0.031	2010 Nov 18	2011 Mar 1
MACSJ1149.6+2223 ^{c,d,e}	MACS1149	11:49:35.86	+22:23:55.0	0.544	0.023	2010 Dec 4	2011 Mar 9
Abell 2261	A2261	17:22:27.25	+32:07:58.6	0.224	0.043	2011 Mar 9	2011 Jun 13
MACSJ1206.2-0847 ^f	MACS1206	12:06:12.28	-08:48:02.4	0.440	0.063	2011 Apr 3	2011 Jul 20
RXJ1347.5-1145	RXJ1347	13:47:30.59	-11:45:10.1	0.451	0.062	2011 Apr 19	2011 Jul 14
MACSJ2129.4-0741 ^{c,d}	MACS2129	21:29:26.06 ^g	-07:41:28.8 ^g	0.570	0.076	2011 May 15	2011 Aug 3
MACSJ0329.7-0211 ^h	MACS0329	03:29:41.68	-02:11:47.7	0.450	0.060	2011 Aug 18	2011 Nov 1
MS2137-2353	MS2137	21:40:15.18	-23:39:40.7	0.313	0.051	2011 Aug 21	2011 Nov 7
MACSJ0717.5+3745 ^{c,d,e}	MACS0717	07:17:31.65	+37:45:18.5	0.548	0.077	2011 Aug 31	2011 Dec 9
MACSJ0744.9+3927 ^c	MACS0744	07:44:52.80	+39:27:24.4	0.686	0.058	2011 Sep 22	2011 Dec 29
MACSJ0647.8+7015 ^{c,d}	MACS0647	06:47:50.03	+70:14:49.7	0.584	0.111	2011 Oct 5	2011 Nov 29
MACSJ1115.9+0129 ^f	MACS1115	11:15:52.05	+01:29:56.6	0.352	0.039	2011 Dec 14	2012 Feb 24
Abell 611	A611	08:00:56.83	+36:03:24.1	0.288	0.057	2012 Jan 28	2012 May 17
RXJ1532.9+3021	RXJ1532	15:32:53.78	+30:20:58.7	0.363	0.030	2012 Feb 3	2012 Apr 12
MACSJ1720.3+3536 ^f	MACS1720	17:20:16.95	+35:36:23.6	0.387	0.038	2012 Mar 26	2012 Jun 17
MACSJ1931.8-2635 ^f	MACS1931	19:31:49.66	-26:34:34.0	0.352	0.110	2012 Apr 10	2012 Jun 25
MACSJ0416.1-2403 ^{d,e,f}	MACS0416	04:16:09.39	-24:04:03.9	0.396	0.041	2012 Jul 24	2012 Sep 27
RXCJ2248.7-4431 ^e	RXCJ2248	22:48:44.29	-44:31:48.4	0.348	0.012	2012 Aug 30	2012 Nov 19

^a The shortened cluster names that are generally used in this paper.

^b Cluster coordinates derived from X-ray data, except where noted.

^c Ebeling et al. (2007).

^d High-magnification cluster.

^e Hubble Frontier Fields (HFF) cluster.

^f Ebeling et al. (2010).

^g Cluster coordinates derived from optical data.

^h Mann & Ebeling (2012).

Table 2
CLASH Filter Selection, Typical Exposure Times, and Limiting Magnitudes

Detector	Filter	<i>HST</i> Orbits	Exposure Time (s) ^a	m_{lim} ^b
WFC3/UVIS	F225W	1.5	3627	26.4
WFC3/UVIS	F275W	1.5	3697	26.5
WFC3/UVIS	F336W	1.0	2381	26.6
WFC3/UVIS	F390W	1.0	2408	27.2
ACS/WFC	F435W	1.0	2036	27.2
ACS/WFC	F475W	1.0	2052	27.6
ACS/WFC	F606W	1.0	2028	27.6
ACS/WFC	F625W	1.0	2015	27.2
ACS/WFC	F775W	1.0	2046	27.0
ACS/WFC	F814W	2.0	4149	27.7
ACS/WFC	F850LP	2.0	4162	26.7
WFC3/IR	F105W	1.0	2754	27.3
WFC3/IR	F110W	1.0	2543	27.8
WFC3/IR	F125W	1.0	2482	27.2
WFC3/IR	F140W	1.0	2323	27.4
WFC3/IR	F160W	2.0	5108	27.5

^a Average exposure times in each filter for the CLASH clusters presented in this paper.

^b Typical 5σ limiting magnitudes in an $r = 0''.2$ circular aperture.

clusters in the CLASH sample. The cluster observations are provided in Table 1 and the exposure details, including filters, exposure times, and limiting magnitudes, for a typical cluster are presented in Table 2. The galaxy cluster sample in this paper includes 11 clusters from the Massive Cluster Survey (MACS; Ebeling et al. 2001), including six at $z < 0.5$ (Ebeling et al. 2010; Mann & Ebeling 2012) and five at $z > 0.5$ (Ebeling et al. 2007). Henceforth, we will refer to the clusters by their shortened names listed in Table 1.

We calibrate the raw *HST* data using standard techniques to remove the instrumental bias, dark, and flat-

field signatures from the data. The ACS data are further processed to remove the bias striping and charge-transfer inefficiency effects. For the WFC3/IR data, we take advantage of “guard darks” taken immediately preceding the first visit of most CLASH observations. Our calibration pipeline subtracts the standard dark from the guard dark to create “delta darks”, which contain information about new hot/warm pixels and persistence of charge from data taken in the orbits immediately prior to CLASH observations. Additionally, we identify bright sources in our WFC3/IR observations to create persistence masks for data taken within CLASH visits. The

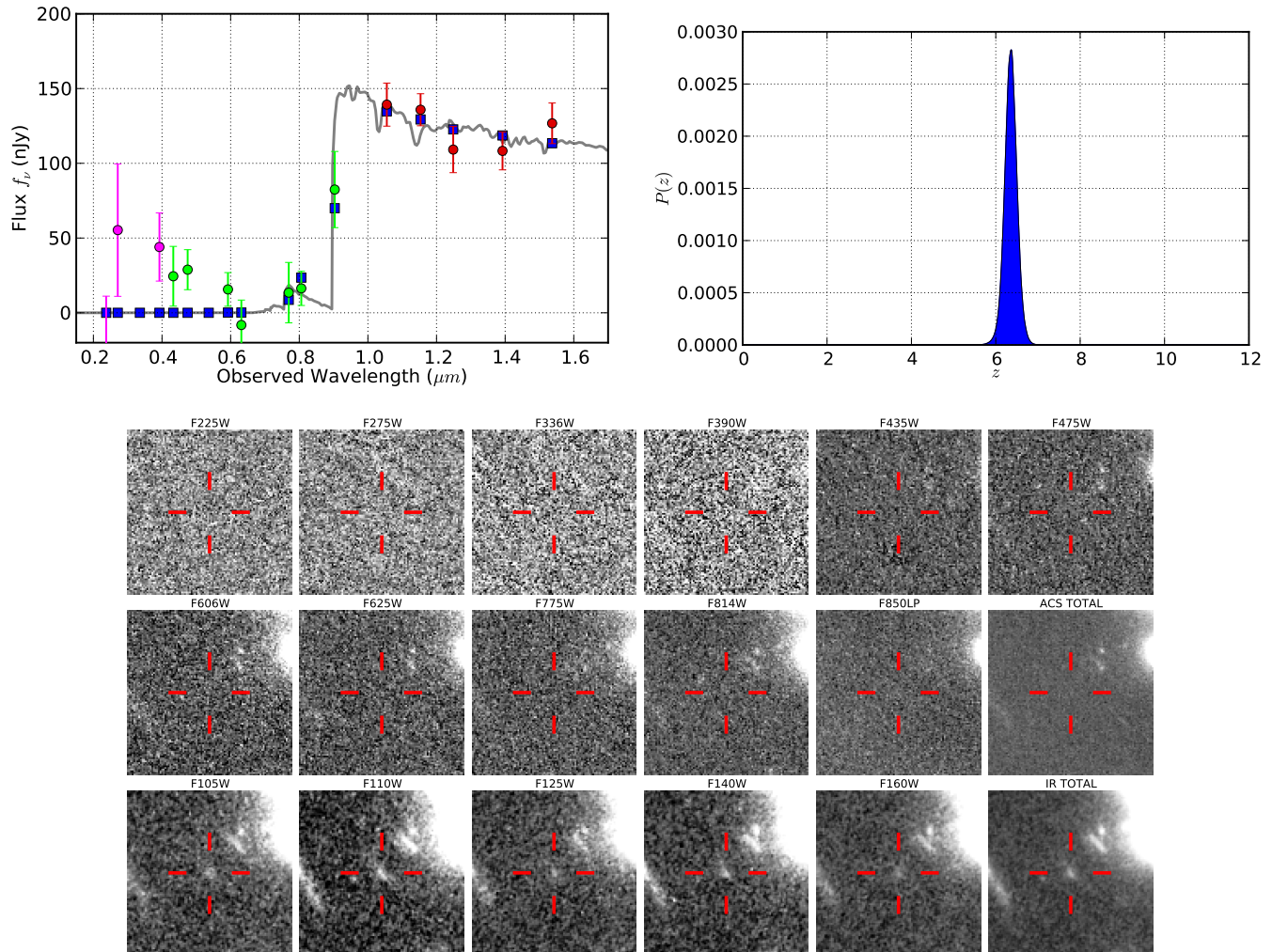


Figure 1. Top left: Observed SED (magenta, green, and red data points with 1σ error bars) and BPZ SED template fit (gray line with blue data points). Top right: Posterior photometric redshift probability distribution. Bottom: multiband postage stamp images for the $z \sim 6.4$ candidate A2261–0754. The field of view of each stamp image is $13''.1 \times 13''.1$ and is shown at a position angle (E of N) of 0° . The stamps marked ACS and IR total represent the inverse-variance weighted sum of all the images taken with those two respective detectors.

external and internal persistence masks are flagged in the WFC3/IR data quality arrays and used downstream to exclude persistence regions when drizzling the data.

The data in each filter were combined with the MosaicDrizzle pipeline (Koekemoer et al. 2003) described in detail in our overview paper (Postman et al. 2012). The pipeline produces cosmic-ray rejected and aligned images for each filter using a combination of cross-correlation and catalog matching. The final images are drizzled to a common pixel grid with a scale of $0''.065 \text{ pixel}^{-1}$.

3. PHOTOMETRY AND SOURCE CATALOGS

We used SExtractor version 2.5.0 (Bertin & Arnouts 1996) in dual-image mode to perform object detection and photometry. For each of our 18 clusters, we constructed a detection image by performing an inverse-variance weighted sum of the images in all five WFC3/IR bands: Y_{105} , J_{110} , J_{125} , JH_{140} , and H_{160} . The local background was measured within a rectangular annulus (default width 24 pixels) and sources were required to be detected at $> 1\sigma$ significance over a minimum area of nine contiguous pixels. We measured object colors

using the flux enclosed within the isophotal apertures. The flux uncertainties are derived by SExtractor using an rms image (input to SExtractor as a weight map) including all sources of noise except for the Poisson noise of the objects. The flux uncertainty derived by SExtractor adds the Poisson source noise in quadrature to the noise determined from the rms image, which is primarily background noise.

Sources that are undetected ($< 1\sigma$) in a particular band are given their 1σ upper detection limit to calculate limits for object colors. Total magnitudes were measured in scalable Kron (1980) apertures with a Kron factor of 2.5 and a minimum radius of 3.5 pixels. Our photometry is also corrected for the foreground Galactic extinction along the line of sight to each cluster using the Schlegel et al. (1998) IR dust emission maps. The $E(B - V)$ color excess values for each cluster are presented in Table 1.

No correction for the varying size of the PSF across the bandpasses has been applied to the CLASH photometric catalogs. For the typical sizes of our high-redshift candidates, applying such a correction would redden the $Y_{105} - H_{160}$ colors by only ~ 0.1 mag. All of the CLASH *HST* data and source photometric catalogs are available

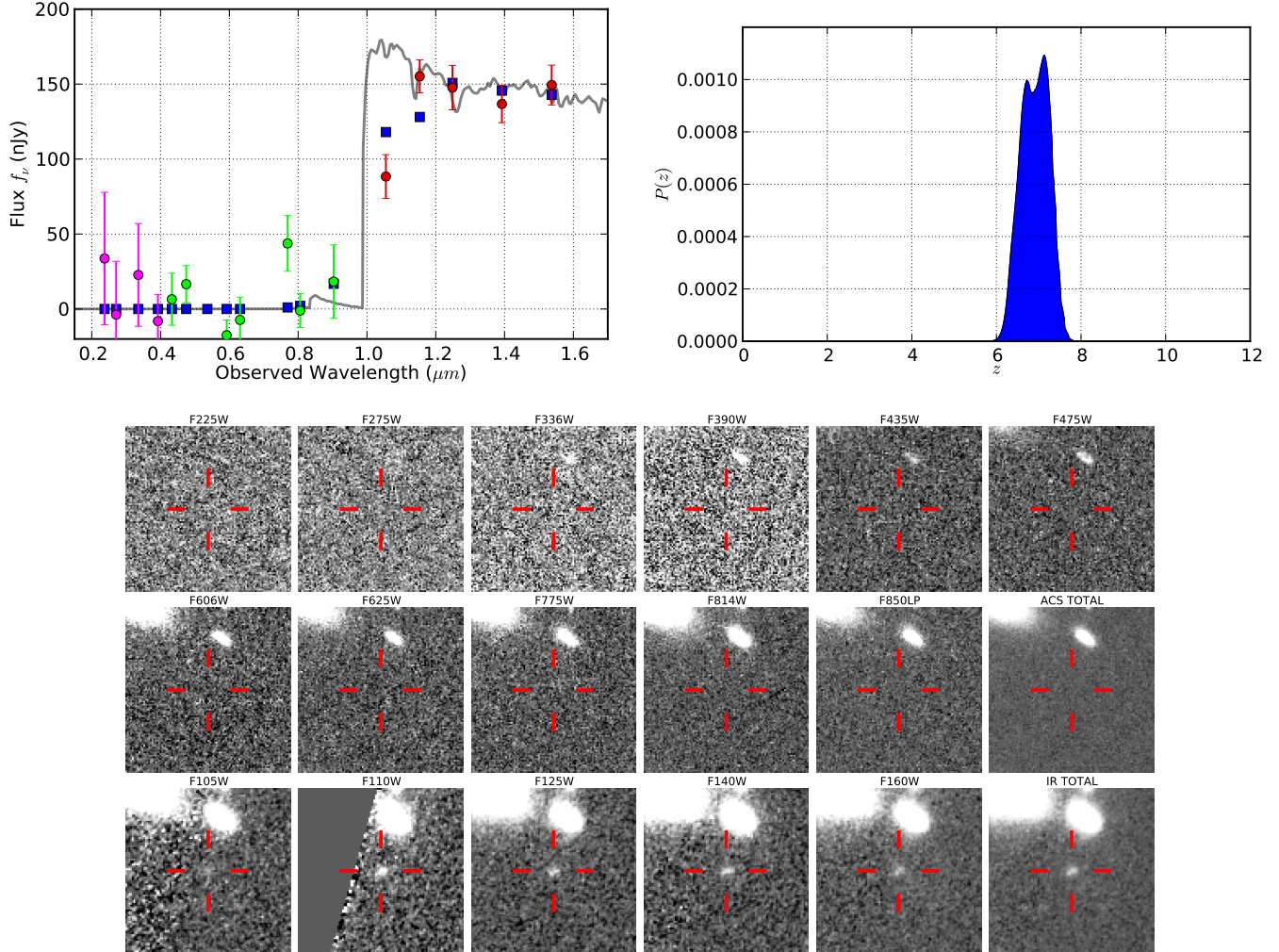


Figure 2. Same as in Figure 1, but for the $z \sim 7.1$ candidate RXJ1532-0844.

online.³¹

It should be noted that the CLASH photometric catalogs do not correct for the presence of correlated noise introduced in the drizzling procedure (e.g., Casertano et al. 2000). However, after we constructed our catalogs and samples of high-redshift candidates, we later investigated the effects of correlated noise on the high-redshift sample selection (see Section 5).

4. PHOTOMETRIC REDSHIFTS

In total, our catalogs contain over 38,000 sources over all the 18 clusters. For each source, we derive photometric redshifts using the complete 16 band (or 17 band) observed photometry spanning from 0.2 to 1.7 μm . To estimate the redshifts of our candidates and to derive the posterior redshift probability distribution functions, $P(z)$, we used the Bayesian photometric redshift (BPZ) code (Benítez 2000; Benítez et al. 2004; Coe et al. 2006).

The photometric redshifts are based on a χ^2 fitting procedure to the observed measured fluxes (even if negative), and flux uncertainties. We utilized a combination of empirical galaxy templates and template SEDs from PEGASE (Fioc & Rocca-Volmerange 1997) that have been recalibrated with known spectroscopic redshifts from the

FIREWORKS survey (Wuyts et al. 2008). BPZ does not redden any of its SED templates, but it includes a large range of templates designed and calibrated to fit almost all galaxies. Comparing BPZ’s template set to large data sets with high-quality spectra reveals that there are only $\lesssim 1\%$ outliers not covered by BPZ. This demonstrates that the BPZ templates encompass the range of metallicities, reddenings, and star formation histories observed for the vast majority of real galaxies (Coe et al. 2013). Lyman series line-blanketing and photoelectric absorption produced by intervening hydrogen along the line of sight are applied to the BPZ templates following the prescription of Madau (1995).

At present, the Bayesian prior, $P(z, m_0)$, is not well calibrated at faint magnitudes ($m \gtrsim 26$) or at the high redshifts $z \sim 6 - 8$ investigated here. Therefore, we utilized a flat prior in BPZ to construct our catalog of high-redshift galaxy candidates. Note that because of the flat prior, the photometric redshifts derived here for the specific purpose of identifying high-redshift galaxy candidates are different from the best-fitting z_{phot} in the online CLASH catalogs. However, for comparison, the online CLASH catalogs include a maximum likelihood redshift, z_{ml} , which is equivalent to using a flat prior. For details about the BPZ priors used in the online CLASH

³¹ <http://archive.stsci.edu/prepds/clash/>

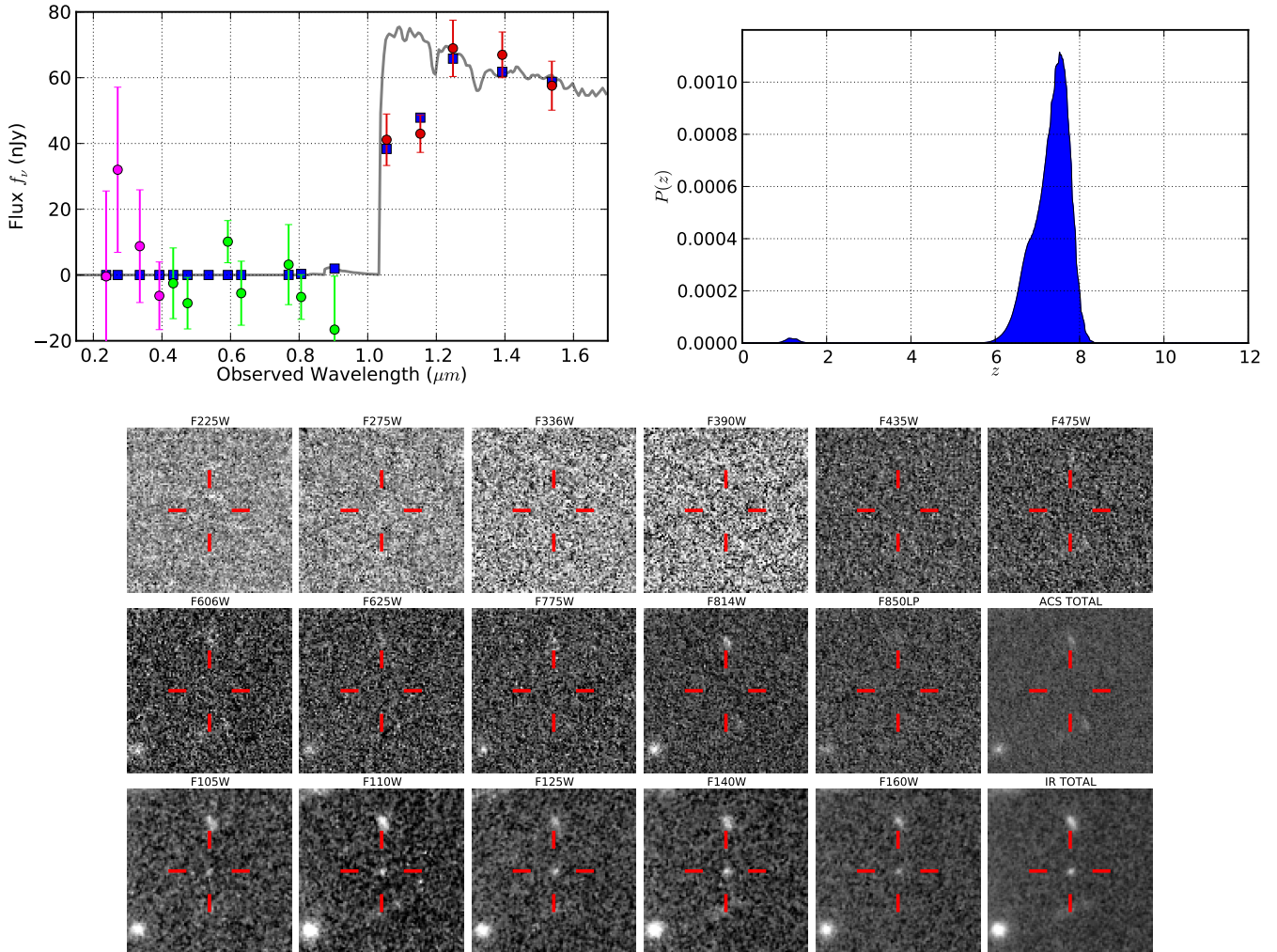


Figure 3. Same as in Figure 1, but for the $z \sim 7.5$ candidate A2261-0187.

catalogs, please see [Jouvel et al. \(2014\)](#).

The primary contaminants to the $z \sim 5.5 - 8.5$ sample are faint red galaxies at $z \sim 1.0 - 1.9$. This class of low-redshift galaxies with very prominent Balmer breaks represents the main galaxy population that can mimic high-redshift LBGs. We can directly compare the expected relative numbers of faint red $z \sim 1 - 2$ galaxies and blue star-forming galaxies at $z \sim 5.5 - 8.5$ using published galaxy luminosity functions (LF) for these two galaxy populations ([Giallongo et al. 2005](#); [Bouwens et al. 2011](#); [Bradley et al. 2012b](#)). We base our low-redshift expectations on [Giallongo et al. \(2005\)](#), who derived LFs for red galaxies using deep NIR observations over the HDF-North and HDF-South fields and the K20 spectroscopic sample ([Cimatti et al. 2002](#)). For high-redshift expectations, we use the LFs derived by [Bouwens et al. \(2011\)](#) and [Bradley et al. \(2012b\)](#).

At $z \sim 1.5$, the [Giallongo et al. \(2005\)](#) $m/m(\text{bimodal})$ LF results correspond to $M_{B,0}^* = -21.62$ mag, $\phi^* = 3.8 \times 10^4 \text{ Mpc}^{-3}$, and $\alpha = 0.53$. Assuming the magnitude range between 26 – 27 mag (where majority of the high-redshift galaxies are to be found) and a selection window with $\Delta z = 1$, the LFs predict 0.18 faint red galaxies per arcmin² at $z \sim 1.5$ and 0.40 $z \sim 7$ galaxies per arcmin². These results suggest that in a

“blank” field we are ~ 2.2 times more like to find a blue high-redshift galaxy than a faint red low-redshift galaxy. This ratio of blue high-redshift to red low-redshift galaxies is even larger in a lensed field because the number density of high-redshift galaxies intrinsically fainter than 27 mag is increasing, while the number density of the $z \sim 1 - 2$ faint red galaxy population is decreasing. As a consequence, our use of a flat redshift prior for the specific task of identifying high-redshift galaxy candidates is conservative and not preferentially selecting high-redshift galaxies (see also Appendix A from [Bouwens et al. 2012a](#), who used a similar argument for the use of a flat prior in the context of $z \sim 9$ sources from CLASH).

5. HIGH-REDSHIFT CANDIDATE SELECTION

5.1. Catalog Construction

We use the photometric redshift catalog to select high-redshift galaxy candidates at redshifts $z > 5.5$. While we do not use a two-color Lyman-break selection technique to select high-redshift galaxies (e.g., [Bouwens et al. 2011](#)), BPZ identifies high-redshift galaxy candidates primarily based on the presence of the Lyman break feature in their SED. BPZ optimally utilizes the photometry in all 16 broadband filters, including UV and optical non-detections or marginal detections, and provides a quanti-

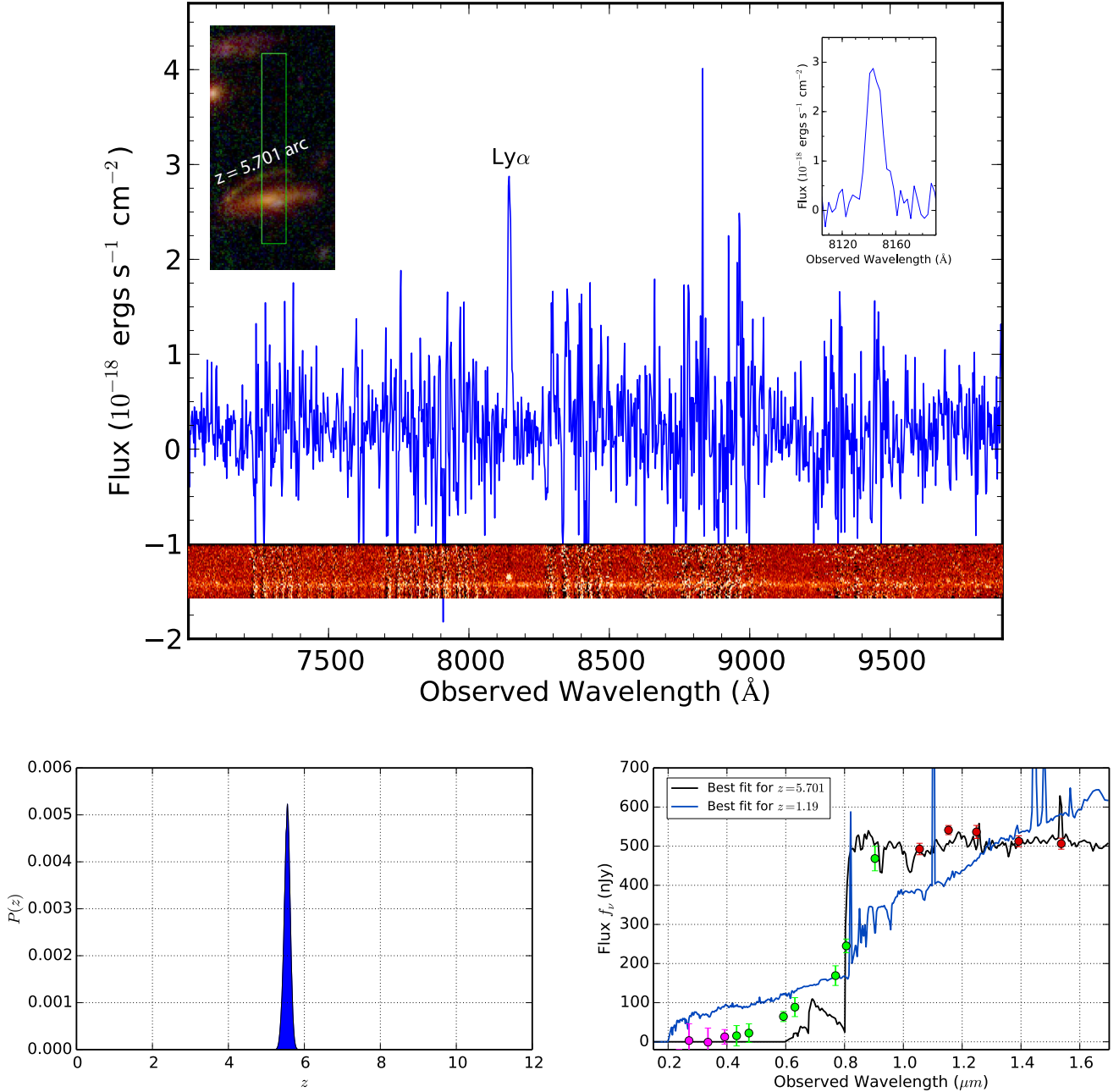


Figure 4. Observed 1D longslit spectrum of MACS1206-1796 ($m_{160} = 23.8$) obtained with *VLT/VIMOS* as part of the CLASH *VLT* program (PI: P. Rosati). The spectrum exhibits a clear emission line at 8146 Å, corresponding to Ly α at $z = 5.701$. The upper-left inset shows the slit location. The upper-right inset shows a close up of the emission line, which shows an asymmetric profile suggestive of Ly α . The 2D spectrum is shown along the bottom of the plot. Bottom left: the posterior photometric redshift distribution of this galaxy. The peak is at $z_{\text{phot}} = 5.6$, which differs from the spectroscopic measurement by only 1.8%. Also note that this galaxy is part of a quadruply-lensed system behind MACS1206 and was predicted to have a redshift of $z = 5.7$ based on the lens model (Zitrin et al. 2012c). Bottom right: the best-fitting BPZ SEDs at the fixed redshifts of $z = 5.701$, assuming the line is Ly α , and $z = 1.19$, assuming the line is [O II] $\lambda\lambda 3727$. The low-redshift solution provides a much poorer fit to the observed photometry. Overall, the evidence suggests that the high-redshift solution is more likely.

tative estimate for the redshift uncertainty. Traditional LBG color–color selections are generally limited to two (or three) bands plus nondetection in the optical. The color–color cuts can exclude genuine high-redshift candidates (for example, the specific Lyman-break color cut chosen necessarily selects objects at different redshift cut-offs due to intrinsic differences in object colors), while possibly including more low-redshift contaminants (e.g., see Finkelstein et al. 2010; Dunlop 2013).

These two alternative approaches to LBG selection have been employed with great success on deep and ultra-deep *HST* fields such as the HUDF. While some groups have used color–color selections (e.g., Oesch et al. 2010b; Bouwens et al. 2011; Bunker et al. 2010; Ellis et al. 2013; Schenker et al. 2013) and others have used photometric-redshift selections (e.g., Finkelstein et al. 2010; McLure et al. 2010, 2013), the resulting $z \sim 7 - 8$ galaxy samples are generally in very good agreement, especially at brighter magnitudes.

To ensure reliable photometric redshifts and to limit the number of possible contaminants due to photometric scatter, we require that our high-redshift candidates are detected at $\geq 6\sigma$ in the combined JH_{140} and H_{160} bands. As demonstrated in Bouwens et al. (2012a), our high-redshift galaxy selections would otherwise be subject to significant contamination ($\gtrsim 25\%$) for sources detected at lower significance levels, especially faintward of 26.5 mag, due the effects of noise on the photometry of other lower-redshift sources. Further, we investigate any BPZ fit solutions that give a non-physical result, such as an elliptical galaxy SED template fit at $z \gtrsim 6$.

A few of our candidates lack coverage in one or more of the WFC3/IR bands because the observations in these filters were obtained at only one *HST* orient to accommodate the CLASH supernova search program. While all of our candidates have coverage in the H_{160} band, if coverage in the JH_{140} band is missing, we applied the 6σ detection threshold to the H_{160} band plus the next available reddest WFC3/IR filter.

One galaxy in our sample, MACS0744-0225, is detected at only 5.5 σ significance in the combined JH_{140} and H_{160} bands. Despite this fact, we include this candidate in our $z \sim 7$ sample because the lensing model for MACS0744 suggests that this source and MACS0744-1695 likely represent a doubly lensed system at $z \sim 6.6$, and hence it is unlikely to be a low-redshift contaminant.

As mentioned in Section 3, the drizzling procedure introduces pixel-to-pixel noise correlations that are not reflected in the output weight or rms maps. The typical correction for the effects of correlated noise involves rescaling the rms map by measuring the empirical noise in “blank” areas of size comparable to the observed galaxies and comparing it with the noise measured from the unscaled rms maps (e.g., Trenti et al. 2011; Bradley et al. 2012b; Guo et al. 2013). After correcting the rms maps for the effects of correlated noise using “empty aperture” measurements on the data in each of the filters, we then investigated the effects of this increased noise on the photometric redshifts. In particular, without the correlated noise correction, the potential concern is that the significance of the UV/optical nondetections, required for the selection of high-redshift candidates, may be underestimated.

We find that the median correction factors for the noise

in the CLASH UVIS and optical data are relatively small at ~ 1.11 and ~ 1.30 , respectively (these values are larger than the simplified formula presented in Casertano et al. 2000). After re-calculating the photometric redshifts with rescaled errors, we find only two galaxies, both in the initial $z \sim 6$ sample, that subsequently were best fit by low-redshift solutions. Thus, we removed both galaxies from our high-redshift sample.

5.2. Resulting High-redshift Candidate Samples

Using our photometric redshift catalogs, we find 204 $z \sim 6$ candidates, 45 $z \sim 7$ candidates, and 13 $z \sim 8$ candidates, for a total of 262 lensed high-redshift galaxy candidates (Table 3). These numbers have been corrected for multiply imaged lensed systems identified by our fiducial lens models (see Section 6). The coordinates, photometry, and photometric redshift estimates for these candidates are presented in Tables 4, 5, and 6. The mean photometric redshifts for our $z \sim 6$, $z \sim 7$, and $z \sim 8$ samples are 5.9, 6.7, and 7.8, respectively.

We have already spectroscopically confirmed a few of these candidates, including a quintuply lensed $z = 6.11$ galaxy behind RXCJ2248 (Balestra et al. 2013; Monna et al. 2014) and a pair of faint galaxies at $z = 6.387$ behind MACS0717 (Vanzella et al. 2014). We aim to spectroscopically confirm even more of these candidates with upcoming observations at several facilities.

Our sample of LBG candidates is the largest sample of magnified star-forming galaxies at $z \sim 6 - 8$ presented to date. Given the general lack of high-quality optical and NIR multiband observations of lensing clusters prior to the CLASH survey, previous studies in this redshift range have typically focused on one or a few spectacular lensed candidates or particular clusters for which multiband optical and NIR data exist.

Such studies include the triply lensed $z \sim 6.4$ candidate behind Abell 2218 (Kneib et al. 2004), the $z \sim 7.6$ candidate behind Abell 1689 (Bradley et al. 2008), a possible $z \sim 7$ candidate behind Abell 2219 and Abell 2667 (Richard et al. 2008, but see also Bouwens et al. 2009), the $z \sim 6$ candidate behind Abell 1703 and two $z \sim 6.5$ candidates behind CL0024+16 (Zheng et al. 2009), four $z \sim 6$ *i*-dropouts (Bradač et al. 2009) and 10 $z \sim 7$ candidates (Hall et al. 2012) behind the Bullet Cluster (1E0657–56), and seven $z \sim 7$ candidates behind Abell 1703 (Bradley et al. 2012a). Lensed candidates in this redshift range previously studied with CLASH data include the doubly imaged $z = 6.027$ candidate behind A383 (Richard et al. 2011), the quadruply lensed $z \sim 6.2$ candidate behind MACS0329 (Zitrin et al. 2012b), a quintuply lensed $z \sim 5.9$ candidate behind RXCJ2248 (Monna et al. 2014), and other studies that briefly mentioned multiply lensed candidates at $z \sim 5.7$ in MACS1206 (Zitrin et al. 2012c) and $z \sim 6$ in MACS0416 (Zitrin et al. 2013b). In total, these studies comprise 31 lensed high-redshift galaxies at $z \sim 6 - 8$. Our CLASH lensed sample of 262 candidates (which includes the five CLASH galaxies from previous studies) represents nearly an order of magnitude increase in the number of lensed star-forming galaxies at $z \sim 6 - 8$.

As an example of a $z \sim 6$ candidate, we plot the observed SED in the 16 observed bands along with the best-fit BPZ template for the $z \sim 6.4$ candidate A2261-0754 in Figure 1. We also show in this figure its posterior

Table 3
Number of High-Redshift Candidates at $z \sim 6$, $z \sim 7$, and $z \sim 8$ and Area Surveyed at $z \sim 6$ at Low, Intermediate, and High Magnification

Cluster	Number of Candidates ^a			Area (arcmin ²) ^b			Total	μ_{med} ^c
	$z \sim 6$	$z \sim 7$	$z \sim 8$	$\mu \leq 2.3$	$2.3 < \mu < 5.4$	$\mu \geq 5.4$		
Abell 383	3	2	1	0.0	3.2	1.2	4.4	4.4
MACSJ1149.6+2223 ^d	12	0	0	0.0	1.2	3.3	4.5	9.8
Abell 2261	10	4	1	1.8	1.8	0.8	4.4	2.5
MACSJ1206.2-0847	11	1	1	1.5	2.0	1.1	4.6	2.9
RXJ1347.5-1145	6	6	1	0.3	1.9	2.1	4.3	5.2
MACSJ2129.4-0741 ^{d,e}	10	3	0	2.3	1.6	0.8	4.7	2.3
MACSJ0329.7-0211	9	3	0	0.4	2.6	1.5	4.5	3.9
MS2137-2353	5	1	0	3.9	0.6	0.3	4.8	1.5
MACSJ0717.5+3745 ^d	15	0	0	0.1	1.7	2.5	4.3	6.5
MACSJ0744.9+3927	17	3	0	0.0	0.7	4.0	4.6	9.4
MACSJ0647.8+7015 ^d	24	7	1	0.02	0.8	3.6	4.4	15.4
MACSJ1115.9+0129	6	1	1	0.9	2.5	1.3	4.6	3.3
Abell 611	4	2	1	3.6	0.9	0.3	4.7	1.6
RXJ1532.9+3021 ^f	16	4	1
MACSJ1720.3+3536	9	2	2	2.7	1.1	0.6	4.4	1.9
MACSJ1931.8-2635	32	4	1	2.6	1.3	0.6	4.5	2.1
MACSJ0416.1-2403	5	2	1	2.7	1.1	0.8	4.6	2.0
RXCJ2248.7-4431	10	0	1	2.8	1.0	0.8	4.6	1.9
Total	204	45	13	25.7	25.9	25.6	76.9	3.4

^a The number of unique high-redshift candidates. Candidates that our cluster models find are likely multiple images are counted only once.

^b WFC3/IR coverage area at $z \sim 6$ at low ($\mu \leq 2.3$), intermediate ($2.3 < \mu < 5.4$), and high ($\mu \geq 5.4$) magnification, defined such that each magnification bin has approximately the same total area over the 18 clusters. We exclude the search area behind the clusters lost as a result of intervening foreground sources. Because of the weak redshift dependence on d_{ls}/d_s between $z \sim 6$ and $z \sim 8$, the areas surveyed at $z \sim 7$ and $z \sim 8$ are very similar to those at $z \sim 6$.

^c Median cluster magnification for $z \sim 6$ over the WFC3/IR coverage area excluding foreground sources.

^d High magnification cluster.

^e This cluster was selected as one of the five CLASH high magnification clusters, but our lens modeling indicates the overall magnification strength of this cluster is more similar to the X-ray selected CLASH clusters.

^f For completeness, we report the high-redshift candidates identified behind this cluster (see Appendix A), but we do not include them in the analysis of this paper given the uncertain nature of the strong lensing model for this cluster (see Section 6).

photometric redshift probability distribution, $P(z)$. The postage stamp images in each of the 16 filters, as well as the total inverse-variance weighted sum of the ACS and IR images, are also illustrated. We also present the same set of plots and images for the $z \sim 7.1$ candidate RXJ1532-0844 (Figure 2) and the $z \sim 7.5$ candidate A2261-0187 (Figure 3).

For the candidate MACS1206-1796, we have obtained a spectrum from *VLT/VIMOS* as part of the CLASH *VLT* program (PI: P. Rosati). The longslit 1D and 2D spectra, obtained in a one hour exposure, are presented in Figure 4. Based on the fiducial lens model for MACS1206 (see Section 6), this relatively bright candidate (observed H_{160} magnitude of 23.8 mag) is likely part of a quadruply lensed system (obj 8.4 in Zitrin et al. 2012d) along with MACS1206-0457, MACS1206-0861, and MACS1206-1135. Because this object is magnified by the cluster by only a factor of ~ 2.1 and given its long curved arc-like morphology and relative brightness, it is most likely being additionally magnified by the neighboring foreground galaxy with $z_{\text{phot}} \sim 1.1$, making it a probable galaxy–galaxy lens candidate. The spectrum of MACS1206-1796 is cleanly separated from the bright foreground object and exhibits a clear emission line at 8146 Å, corresponding to Ly α at $z = 5.701$. An alternative possibility is that this emission line represents [O II] $\lambda\lambda 3727$ at $z = 1.186$. However, the photometric redshift of this galaxy, based on the 16 band photometry, is $z_{\text{phot}} = 5.6$, which differs from the $z = 5.701$ spectro-

scopic hypothesis by only 1.8% (likely demonstrating the reliability of the photometric redshifts). Moreover, this probable quadruple-lens system was predicted to have a redshift of $z = 5.7$ based on the lens model (Zitrin et al. 2012c).

In Figures 6, 7, 8, 9, and 10, we indicate the positions of our high-redshift candidates within the field of view of the cluster images. In these figures, we also plot the approximate location of the critical curves at $z \sim 6$ based on the fiducial lens models we constructed for these clusters (see Section 6).

In Figure 5, we present histograms of both the observed and intrinsic (unlensed) rest-frame UV magnitudes at ~ 1750 Å for our sample of $z \sim 6$, $z \sim 7$, and $z \sim 8$ high-redshift galaxy candidates identified behind the 17 galaxy clusters (excluding RXJ1532). The intrinsic magnitude of each high-redshift candidate has been calculated using the magnification estimates from the detailed lens models of each cluster. The highest magnifications, and hence the faintest intrinsic magnitudes, usually have the largest magnification errors due to typical uncertainties in the precise location of the critical curves (see Section 6.2). Therefore, we separate the intrinsic magnitude histograms for candidates with magnifications < 5 and ≥ 5 . Because of the strong lensing effect, the intrinsic magnitudes in the relatively shallow CLASH survey (5σ limiting magnitude of ~ 27.5 mag in the H_{160} band) reach deeper (> 29.5 AB mag) than the ultra-deep HUDF12 observations. Our observations

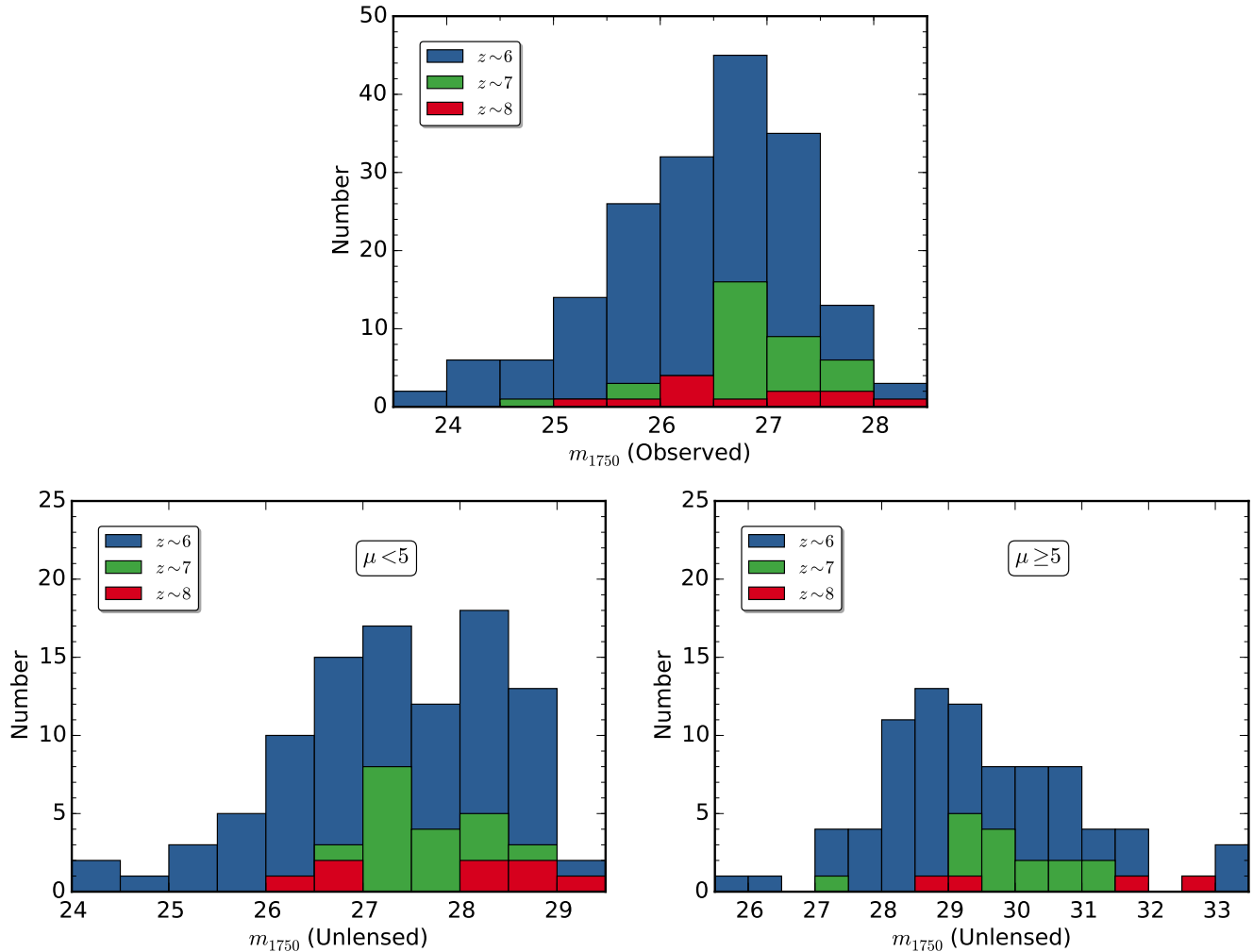


Figure 5. Histogram of the observed (top) and intrinsic (unlensed) (bottom left and right) rest-frame UV magnitudes at $\sim 1750 \text{ \AA}$ for our sample of $z \sim 6$ (blue), $z \sim 7$ (green), and $z \sim 8$ (red) galaxy candidates identified behind 17 CLASH clusters. The highest magnifications, and hence the faintest intrinsic magnitudes, usually have the largest magnification errors due to typical uncertainties in the precise location of the critical curves (see Section 6.2). Therefore, we separate the intrinsic magnitude histograms for candidates with magnifications $\mu < 5$ (bottom left) and $\mu \geq 5$ (bottom right). Because of the strong lensing effect, the intrinsic magnitudes in the relatively shallow CLASH survey (5σ limiting magnitude of ~ 27.5 mag in the H_{160} band) reach deeper (> 29.5 AB mag) than the ultra-deep HUDF12 observations. Our observations of the 17 clusters cover a total area of ~ 22.9 arcmin² with magnifications $\mu > 6.3$, needed to surpass the depth of the HUDF12 observations. This is a relatively robust measure of area in spite of the model uncertainties (see Section 6.3).

of the 17 clusters cover a total area of ~ 22.9 arcmin² with magnifications $\mu > 6.3$, needed to surpass the depth of the HUDF12 observations. This is a relatively robust measure of area in spite of the model uncertainties (see Section 6.3).

5.3. Possible Contaminants

Supernovae, extreme emission-line galaxies (EELG), low-mass stars, and photometric scatter of red low-redshift galaxies can all be sources of contamination for high-redshift galaxy selections. Given that our UV and optical observations of the cluster fields were obtained over the same extended time period (typically $\sim 2 - 3$ months) as the WFC3/IR observations, we can rule out the possibility of contamination from supernovae.

Because we observe each cluster in 16 overlapping broadband filters spanning from 0.2 to $1.7 \mu\text{m}$, contamination from low-redshift extreme emission-line galaxies (e.g., van der Wel et al. 2011; Atek et al. 2011) is minimized in our high-redshift samples. We find two

$z \sim 6$ sources, MACS1115-0352 and MACS1720-1114, with very blue SEDs for which we cannot completely rule out the EELG possibility. The EELG hypothesis would require rest-frame equivalent widths of $\sim 2000 \text{ \AA}$ in $[\text{O III}] \lambda\lambda 4959, 5007$ and $\text{H}\alpha$, but without any substantial $[\text{O II}] \lambda\lambda 3727$ emission, which falls in our i_{775} and I_{814} bands where we have no significant detections (blueward of the Lyman break for a $z \sim 6$ candidate). This possibility and a more general search for EELGs in CLASH data is further explored in X. Huang et al. 2014 (submitted).

In principle, the large number of overlapping filters in CLASH also allows for robust discrimination of low-mass stars, which can be identified by their distinct colors. However, the photometric-redshift code BPZ does not employ stellar templates. To further investigate this possible source of contamination for our unresolved sources, we used the photometric-redshift code LePhare (Arnouts et al. 1999; Ilbert et al. 2006).

LePhare is a SED fitting code that estimates photometric redshifts with a χ^2 fitting method to fit the observed fluxes with template spectra. The code allows us to fit the photometry using galaxy, QSO, and stellar SED templates. The resulting galaxy solutions include the redshift probability distribution function (PDF(z)) and also a secondary solution from the PDF(z), if available. For the galaxy templates, we adopt the COSMOS library (Ilbert et al. 2009), which includes 31 templates of ellipticals, spirals, and starburst galaxies. To take into account the extinction due to the interstellar medium (ISM), we apply the Calzetti (Calzetti et al. 2000) extinction law to the starburst templates and the Small Magellanic Cloud Prevot law (Prevot et al. 1984) to the Sc and Sd galaxy templates. We also allow for inclusion of emission lines in the SED fitting. For stellar templates, we include the Pickles stellar library (Pickles 1998), which include all the normal spectral types plus metal-poor F–K dwarfs and G–K giants, and cool M, L, T dwarf star templates from (Cushing et al. 2005) and Rayner et al. (2009).

In general, it is very difficult to differentiate between extended and point sources at fainter magnitudes. Of course high-redshift galaxies also become smaller and more compact at higher redshifts (e.g. Ferguson et al. 2004; Bouwens et al. 2004; Oesch et al. 2010a; Grazian et al. 2012; Ono et al. 2013), and in fact may be unresolved even in lensed images at *HST* resolution. For example, the lensed ($\mu = 5.2^{+0.3}_{-0.9}$) $z_{\text{phot}} \sim 7$ candidate A1703-zD6 behind Abell 1703 is unresolved in *HST* WFC3/IR data (Bradley et al. 2012a). This galaxy was subsequently confirmed with Keck spectroscopy to be at $z = 7.045$ (Schenker et al. 2012) and to date remains the highest-redshift lensed galaxy with a spectroscopic confirmation.

Based on an empirical PSF model constructed from stars in the cluster fields, we define candidates to be unresolved if they have a FWHM $< 0''.22$ in H_{160} . The unresolved candidates are indicated in Tables 4, 5, and 6, but most of our high-redshift candidates appear to be resolved. The brightest observed object in our catalog (MACS0416-2028, $H_{160} = 23.6$, $\mu \sim 1.5$) is unresolved and despite having a best-fit photometric redshift of $z_{\text{phot}} = 7.2$, we suspect this object is most likely a star. Based on our current understanding of the $z \sim 7$ LF (e.g., Bouwens et al. 2011), the probability of detecting a slightly magnified $z \sim 7$ galaxy with $H_{160} = 23.6$ in the small area covered by the clusters in this paper is exceedingly small. For completeness, we include this candidate in the object tables but do not use it for subsequent analysis given its suspect nature.

Using LePhare, we find that only six of our unresolved candidates have a good fit with stellar templates, with χ_{star}^2 lower than χ_{galaxy}^2 . Another five candidates have χ_{star}^2 comparable to χ_{galaxy}^2 . Therefore, we conclude that the contamination rate from low-mass stars is relatively low at $\lesssim 4\%$, consistent with other studies (e.g., Bouwens et al. 2011). We note these candidates in Table 4. We also note that LePhare slightly prefers a low-redshift galaxy solution ($z \sim 1$) over the high-redshift solution for three of these candidates: A2261-0309, MACS1931-0938, and MACS0647-1670. Given this and the possible fit with stellar templates, these candidates should be considered less confident than the others, even though BPZ

prefers a high-redshift solution.

As discussed earlier, the most significant source of contamination to high-redshift galaxy samples are faint red galaxies at $z \sim 1 - 2$ that enter the sample due the effects of noise on the photometry. Based on simulations in which we add photometric errors to a sample of low-redshift galaxies at $z \sim 1 - 2$, generate a random realizations of the photometry within the error bars, and then recalculate the photometric redshifts using BPZ, we find a low contamination fraction of $< 12\%$ by low-redshift interlopers. Further evidence of a low contamination fraction comes from the distribution of rest-frame UV colors of our $z \sim 6 - 8$ candidate samples, which is much bluer than one would infer for a $z \sim 1 - 2$ red galaxy sample.

6. CLUSTER LENS MODELS

In the framework of the CLASH program, detailed lensing models are being constructed for all 25 CLASH clusters and will eventually be supplied as high-end science products for the community. As the lens modeling is exhaustive and in progress, we use the models available to date to estimate objects magnifications and to assess the possibilities of multiply lensed high-redshift candidates. The detailed mass models are all constructed using either the modeling method of Zitrin et al. (2009) (see also Broadhurst et al. 2005 and other examples in Zitrin et al. 2011, 2012b) or using a second common parameterization of Pseudo Isothermal Elliptical Mass Distributions (PIEMD) for the galaxies, plus elliptical NFW distributions for the dark-matter halos (e.g., Zitrin et al. 2013b,a, on MACS0416 and El Gordo). The first method consists of four to six basic free parameters, explained below. Its main advantage is that the parameterization allows us to readily find multiple-image systems physically, using the preliminary mass model, which is relatively already well constrained. Once multiple images are found the model is refined and the best-fit model is obtained either by a multi-dimensional grid minimization or an Markov Chain Monte Carlo (MCMC) method.

Briefly, the adopted model parameterization is as follows. Galaxies located on the cluster’s red sequence are identified as cluster members and are modeled using a power-law surface mass density, scaled by their apparent luminosity. The individual galaxy contributions are then added to represent the overall galaxy contribution to the total deflection field. The superposed mass distribution of the galaxies is then smoothed, with either a 2D spline interpolation or a Gaussian kernel, to obtain a light-traces-mass representation of the smooth dark matter component. These two components are then added with a relative scaling to adjust for the relative contribution of galaxies to the total mass and then the overall added deflection field is normalized to the corresponding lensing distance. In addition, it is often useful to introduce an external shear imitating ellipticity so that more flexibility is allowed when fitting the location of multiple images. For full details on the cluster lens modeling procedure, see Zitrin et al. (2009).

The second method is similar in essence to the first method, but the main difference in the parameterization is that the DM is represented by an analytical form, specifically an elliptical NFW profile (i.e., it is no longer represented by a smooth version of the galaxy light). Compared to the first parameterization, this method is

less coupled to the light distribution and can give better fits to the data.

Each method has its own advantages and disadvantages and both methods are well common in the literature. A more explicit comparison was discussed in several recent works such as (Zitrin et al. 2013b,a), modeling MACS0416 and El Gordo, respectively. The underlying systematics can be also assessed further by comparing a wider range different lens models as is now being done in the Frontier Fields program,³² which includes our own models. We typically estimate these systematics at the 10%–20% level in regions not too close to the critical curves where the magnification diverges. We are in the progress of quantifying the accuracy of these methods in more detail (A. Zitrin et al. 2014, in preparation).

We have constructed detailed lensing models for 17 of the 18 clusters in this paper. Ten of these models were constructed with the “light traces mass” technique, which excels in approximating the mass distribution even with very few constraints because of the underlying coupling to the light distribution. The remaining seven were constructed using the PIEMD parameterization. We exclude RXJ1532.9+3021 because we have not been able to clearly identify any multiply imaged galaxies that are required to constrain the strong lensing model. Therefore, we do not further discuss the high-redshift candidates behind RXJ1532 in this paper. They are listed in Appendix A for reference.

The 17 cluster models include the published mass models for Abell 383 (Zitrin et al. 2011), MACS1149 (Zheng et al. 2012), Abell 2261 (Coe et al. 2012), MACS1206 (Zitrin et al. 2012c, also see an alternative CLASH model in Eichner et al. 2013), MACS0329 (Zitrin et al. 2012b), MACS0717 (Medezinski et al. 2013), MACS0647 (Coe et al. 2013), and MACS0416 (Zitrin et al. 2013b). The unpublished lens models are for the clusters RXJ1347, MACS2129, MS2137, MACS0744, MACS1115, Abell 611, MACS1720, MACS1931, and RXCJ2248 (see also Momma et al. 2014 for an alternate CLASH model).

6.1. Magnifications

We show the approximate critical lines, where the magnification is formally infinite, at $z \sim 6$ for these clusters as the white contours in Figures 6 – 9. Because of the very small redshift dependence on the angular diameter distance ratio d_{ls}/d_s at $z \gtrsim 6$, the critical curves for $z \sim 7$ and $z \sim 8$ are similar in shape, but move slightly outward from those shown for $z \sim 6$. At $z = 0.44$, the mean redshift of the clusters explored in this paper, the relative distance ratio d_{ls}/d_s is only 2% higher at $z = 8$ than at $z = 6$.

We utilize the detailed cluster lens models to estimate the magnifications of our high-redshift candidates, which are presented in Tables 4, 5, and 6. For the few candidates that are located outside of the modeled region, we assign a magnification of $\mu = 1.1$, which is typically correct to a few percent given their large radial distances from the cluster center. The median magnifications from the models are 4.2, 4.2, and 4.5 for the $z \sim 6$, $z \sim 7$, and $z \sim 8$ samples, respectively, over an average area of 4.5 arcmin² per cluster. In total, nine of our high-redshift

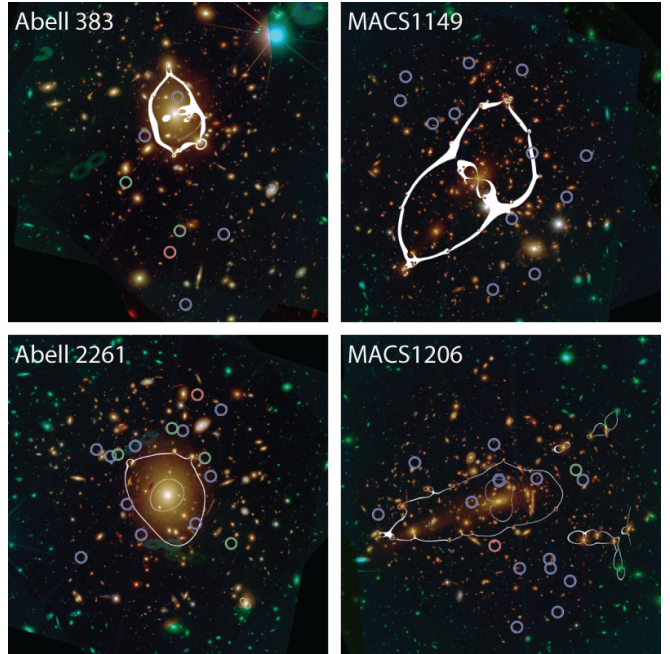


Figure 6. ACS+IR color images of the galaxy clusters A383, MACS1149, A2261, and MACS1206. The field of view of each image is $3'25 \times 3'25$ and is shown with North up and East left. The locations of our high-redshift candidate galaxies at $z \sim 6$, $z \sim 7$, and $z \sim 8$ are marked by the blue, green, and red circles, respectively. The white contours denote the approximate location of the critical lines ($\mu > 200$) at $z \sim 6$ calculated from our fiducial lensing models. MACS1149 is part of the HFF program.

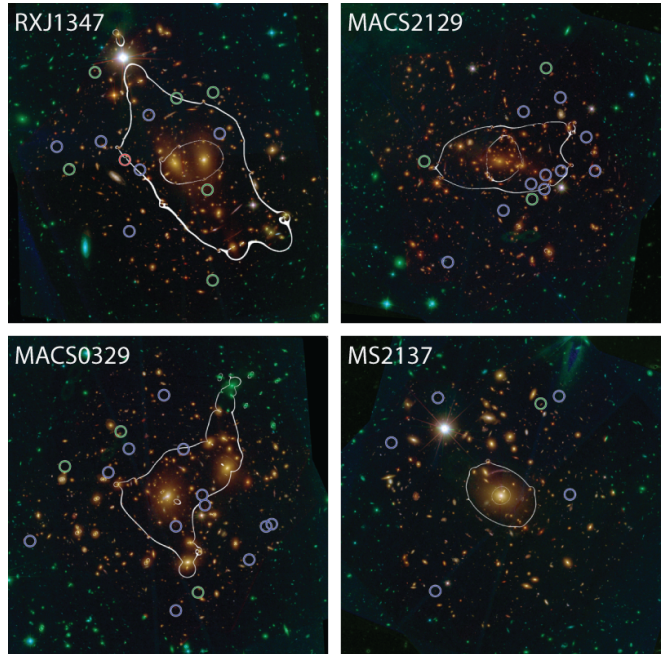


Figure 7. Same as in Figure 6, but for the galaxy clusters RXJ1347, MACS2129, MACS0329, and MS2137.

candidates have estimated magnifications of $\mu > 100$ (i.e., amplifications of > 5 mag) as a result of their close proximity to the critical lines. However, as discussed in Section 6.2, we emphasize that these magnification factors have enormous uncertainties. A small change in the precise location of the critical curve can result in a large but localized inherent uncertainty in the magnification

³² See <http://archive.stsci.edu/prepds/frontier/lensmodels/>.

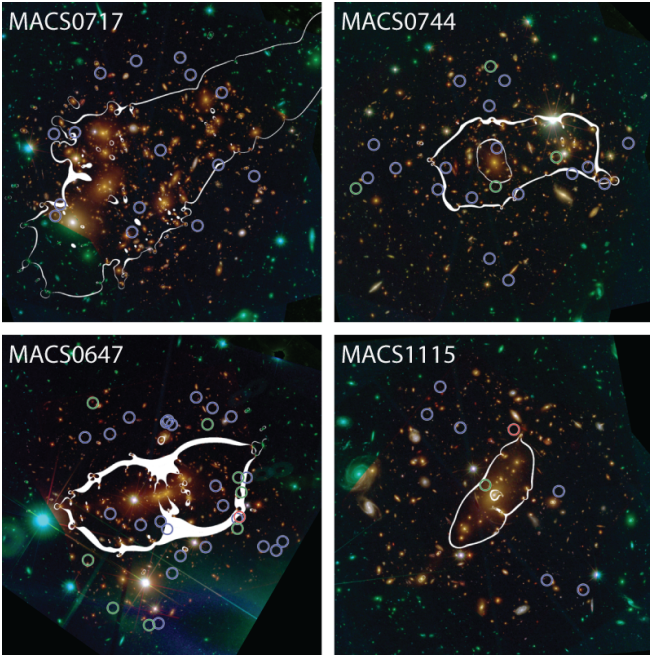


Figure 8. Same as in Figure 6, but for the galaxy clusters MACS0717, MACS0744, MACS0647, and MACS1115. MACS0717 is part of the HFF program.

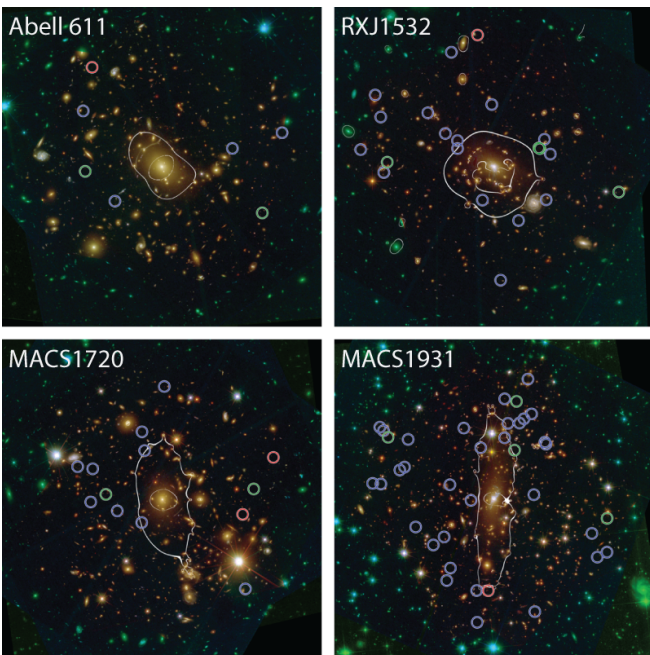


Figure 9. Same as in Figure 6, but for the galaxy clusters A611, RXJ1532, MACS1720, and MACS1931. For RXJ1532, we have not identified any multiply-imaged galaxies, and therefore the critical curve shown is from an approximate lens model based on the light distribution (see Appendix A).

of a few select objects.

6.2. Magnification Uncertainties

To estimate the magnification uncertainties, we tested our ability to accurately measure magnifications given a test case of a simulated lensing cluster. The cluster is “g1” from the numerical–hydrodynamical simulations discussed in Saro et al. (2006). This cluster is

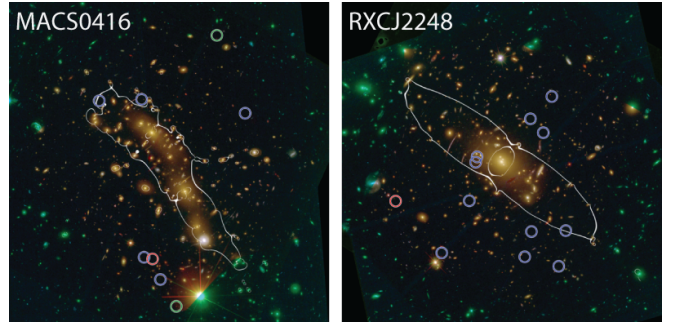


Figure 10. Same as in Figure 6, but for the galaxy clusters MACS0416 and RXCJ2248. Both of these clusters are part of the HFF program.

also part of the sample investigated in Meneghetti et al. (2010), where simulated observations of this cluster with the SkyLens software (Meneghetti et al. 2008) are presented. Based on our analysis of the simulated images, we correctly identified the strongly lensed images of eight background galaxies, spanning the redshift range 1.1 - 3.7. We modeled the strong lensing using the Zitrin et al. (2009) method, then compared our magnification map to the “true” magnification map from the simulated lensing (Figure 11).

Consistent with previous work (Bradač et al. 2009; Maizy et al. 2010), we found the magnification uncertainties increase, in general, as a function of magnification. However, we find larger uncertainties, as the aforementioned study primarily investigated the uncertainties due to low-mass cluster substructure not included in the lens models. We find that large model magnifications > 30 are most likely to be significantly overestimated ($\gtrsim 1\sigma$), as the lens model critical curves (regions of formally infinite magnification) are offset by $\sim 3''$ from their true location, which is impossible to deduce given the lack of multiple images around these positions. This affects only a small percentage of our high-redshift candidates, 10%, 8.5%, and 15% of our $z \sim 6$, $z \sim 7$, and $z \sim 8$ samples, respectively. In addition, we warrant that while our method assumes light traces mass, the simulations have a different way of assigning the light to halos, which renders the presented comparison not pure. Tests of additional simulated clusters are required to confirm these levels of uncertainties as a more general result.

6.3. Total Observed Area as a Function of Magnification

In Figure 12, we plot the total area over the 17 clusters as a function of the magnification factor. Because of the very small redshift dependence on d_{ls}/d_s between $z \sim 6$ and $z \sim 8$ (see Section 6), the areas at $z \sim 7$ and $z \sim 8$ are very similar to those at $z \sim 6$. One consequence of this effect is that the search volumes behind these clusters is relatively insensitive to redshift, allowing for a differential determination of UV LF with lower overall uncertainties. Bouwens et al. (2012a) use three lensed $z \sim 9$ candidates in CLASH and take advantage of this effect to derive the UV LF at $z \sim 9$ based on the well-determined $z \sim 8$ LF determined from the HUDF09+ERS deep fields (Bouwens et al. 2011).

Further, while local magnifications close to the critical curves can have large uncertainties, the overall shape of this total area versus magnification curve, which is critical in deriving lensed UV LFs (see Section 7), is not

significantly affected by uncertainties in lensing models. Because the model constraints, which are the multiple images and their redshifts, are not changed, the area of high magnification is well known and is not very sensitive to the exact position of the critical curves. To surpass the HUDF12 depth, we need to extend our limiting magnitude by 2 mag, which corresponds to a magnification $\mu > 6.3$ (shaded area in Figure 12). We estimate that our observations of 17 clusters cover a total area of 22.9 arcmin² where $\mu > 6.3$.

Due to the strong lensing effect, several regions in the observed image plane can map back to the same area in the source plane at high redshift. However, the redundant search area reduces the effective search areas by only $\sim 10\%$.

6.4. Multiply Lensed Systems

Using the lensing models described above, we find seven likely multiple image systems between $z \sim 5.5 - 8.5$ in the clusters examined here. These multiple systems are noted in Tables 4, 5, and 6. They include the spectroscopically confirmed $z = 6.027$ system in Abell 383 (Richard et al. 2011), the quadruply lensed galaxies at $z \sim 6.2$ in MACS0329 (Zitrin et al. 2012b) and at $z = 5.701$ in MACS1206 (Zitrin et al. 2012c), a doubly lensed galaxy at $z \sim 6$ in MACS0416 (Zitrin et al. 2013b), and a quintuply lensed $z \sim 5.9$ galaxy in RXCJ2248 (Monna et al. 2014), which have been spectroscopically confirmed at $z = 6.11$ from our CLASH-VLT program (Balestra et al. 2013). We have also identified two new doubly lensed multiple systems: one at $z \sim 6.5$ in MACS0647 and one at $z \sim 6.6$ in MACS0744. This represents the largest sample of multiply imaged LBGs at $z > 5.5$ presented to date. For completeness, we also note that the $z \sim 10.7$ candidate behind MACS0647 is also a multiple-image system with three separate images (Coe et al. 2013) that help to make this the most robust candidate at $z > 10$.

7. OBSERVED NUMBER DENSITIES OF STAR-FORMING GALAXIES AT $z \sim 6 - 8$

Gravitational lensing allows us to reach much deeper limiting magnitudes ($\sim 2.0 - 2.5$ mag over large areas), thus revealing a previously unseen population of intrinsically faint star-forming galaxies. However, there is an important tradeoff to consider with lensing searches. The magnification effect also reduces the effective source plane area at high-redshift inversely proportional to the magnification ($A \sim \mu^{-1}$), which in turn reduces the search volume behind the cluster. Therefore, the overall efficiency of cluster lensing searches depends critically on the slope of the galaxy luminosity function at faint magnitudes.

The trade-off between depth and area is such that the surface density should be enhanced over the field where the galaxy UV LF is steep ($-d(\log \phi)/d(\log L) > 1$), and reduced where the LF is shallower (Broadhurst et al. 1995). The effective slope at the bright end (the exponential cutoff region for $L > L_*$) of the $z \sim 6 - 8$ LFs is sufficiently steep such that the surface density of bright high-redshift candidates should be higher behind lensing clusters than in field surveys. This effect is dependent on magnification such that higher magnification regions

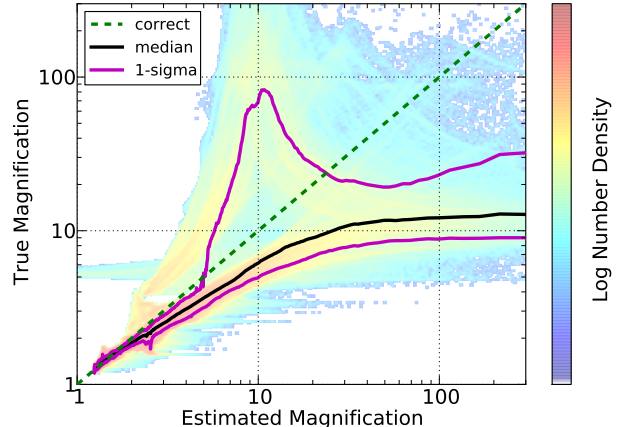


Figure 11. Results from lens modeling of a simulated cluster: true vs. estimated magnifications. Values are compared at every $0''.05$ pixel within a $2'.5 \times 2'.5$ field of view and the density of points is plotted here. The correct magnification values fall along the green dashed line. The median and 68% intervals are plotted as solid black and magenta lines, respectively. For example, an estimated magnification of five likely corresponds to a true magnification between three and five at 68% confidence. Estimated model magnification values greater than 30 are often large overestimates, as the lens models do not precisely reproduce the locations of the critical curves.

should exhibit higher number densities than lower magnification regions.

At fainter magnitudes, in the power-law regime of the UV LF (i.e., $L < L_*$), one would expect the number counts to be diminished because of the reduction in effective volume at high redshift. However, the observed faint-end slopes recently derived for UV LFs at $z \sim 6 - 8$ (Bouwens et al. 2011; Oesch et al. 2012; Bradley et al. 2012b; Schenker et al. 2013; McLure et al. 2013) are very steep, e.g., $\alpha = 1.98 \pm 0.2$ at $z \sim 8$ (Bradley et al. 2012b) corresponding to a $-d(\log \phi)/d(\log L)$ effective slope of ~ 1 . The consequence of the very steep faint-end slopes is that the number densities behind lensing clusters at faint magnitudes should be very similar or slightly higher than those found in blank fields to the same limiting magnitude.

Using our sample of high-redshift lensed candidates and detailed cluster lensing models, we can compare our number densities with expectations for lensed fields. The UV LF has been robustly derived for “blank” fields at $z \sim 6 - 7$ from deep *HST* observations of the GOODS-S, HUDF09, HUDF12, ERS, and CANDELS fields. Here we utilize the results from Bouwens et al. (2007) and Bouwens et al. (2011) based on the GOODS-S, HUDF, and ERS fields. At $z \sim 6$, Bouwens et al. (2007) derive a UV LF with a normalization $\phi^* = 1.4_{-0.4}^{+0.6} \times 10^{-3}$ Mpc⁻³, a characteristic rest-frame UV absolute magnitude of $M_{UV}^* = -20.24 \pm 0.19$, and a faint-end slope of $\alpha = -1.74 \pm 0.16$. At $z \sim 7$, Bouwens et al. (2011) find $\phi^* = 0.86_{-0.39}^{+0.7} \times 10^{-3}$ Mpc⁻³, $M_{UV}^* = -20.14 \pm 0.26$, and $\alpha = -2.01 \pm 0.21$.

Combining the *HST* WFC3 pure-parallel BoRG observations, which constrain the bright end of the UV LF, with the deeper HUDF09+ERS data, Bradley et al. (2012b) derived the $z \sim 8$ UV LF over a very wide dynamic range in magnitude. The combined data sets are

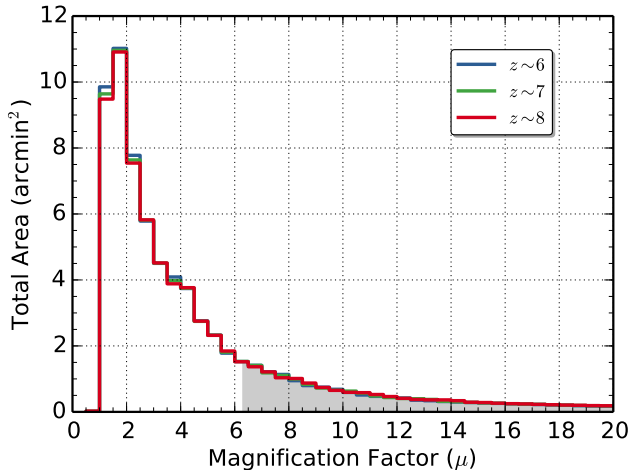


Figure 12. Total search area over the 17 clusters as a function of magnification at $z \sim 6$ (blue), $z \sim 7$ (green), and $z \sim 8$ (red). Because the redshift dependence on d_{ls}/d_s between $z \sim 6$ and $z \sim 8$ is very small (see Section 6), the total areas are very similar in each of the three redshift bins. One consequence of this effect is that the search volumes behind these clusters is relatively insensitive to redshift, allowing for a differential determination of the UV LF with lower overall uncertainties (Bouwens et al. 2012a). While local magnifications close to the critical curves can have large uncertainties, the overall shape of this total area vs. μ curve is not significantly affected by uncertainties in lensing models. The gray shaded region denotes the area with magnifications $\mu > 6.3$, which extends our limiting magnitude by 2 mag and corresponds to regions deeper than the HUDF12 observations.

well fitted by a Schechter function with $\phi^* = 4.3^{+3.5}_{-2.1} \times 10^{-4} \text{ Mpc}^{-3}$, $M_{UV}^* = -20.26^{+0.29}_{-0.34}$, and $\alpha = -1.98^{+0.23}_{-0.22}$.

In Figure 13, we plot these field UV LFs with their uncertainties as the red curves. The expected field number counts are derived using the total area covered by the lensing clusters. Using the SExtractor object segmentation maps, we exclude the search area behind clusters lost as a result of intervening foreground sources. We find a total area of 76.9 arcmin^2 over the 17 clusters.

We then convolve the UV LFs at $z \sim 6$, $z \sim 7$, and $z \sim 8$ through our strong lens models of the 17 clusters. This procedure accounts for both effects of brightening the sources and the reduction in search area with magnification. These effects are encapsulated by the total observed area in each magnification bin (see Figure 12), which is relatively insensitive to the magnification uncertainties. The resulting expected lensed field number counts are plotted with their uncertainties in Figure 13 as the blue curves. We include the lens model uncertainties, estimated from our analysis of simulated lensing (Section 6.2), which we find to be subdominant to Poisson uncertainties.

As a result of the apparent increased steepness of the faint-end slope of the UV luminosity function at $z \sim 7 - 8$ with $\alpha \sim -2.0$, we find that lensing clusters are more efficient than blank field surveys in searching for $z \gtrsim 7$ galaxies down to at least 29 AB mag. At $z \sim 6$, where the faint-end slope is relatively shallower with $\alpha \sim -1.75$, it appears that lensing clusters are more efficient than field surveys at the bright end down to ~ 27 AB mag. Fainter than 27 AB mag, field surveys at $z \sim 6$ appear to be only marginally more efficient than lensing surveys down to at least 29 AB mag.

In Figure 13, we also plot our observed number counts,

with 68% (1σ) confidence intervals for a Poisson distribution, for our lensed galaxy samples at $z \sim 6$, $z \sim 7$, and $z \sim 8$. Our number counts have been corrected for an estimated contamination fraction of 12% (see Section 5.3). To estimate the effects of photometric scatter on the photometric-redshift completeness of our samples, we performed Monte Carlo simulations by generating 1000 random realizations of each high-redshift galaxy in our sample within its 1σ photometric errors in each band. We then run BPZ on the randomly generated photometry and determine the derived photometric redshifts to estimate our completeness as a function of observed magnitude.

As can be seen in the figure, the observed number counts of our lensed high-redshift sample are roughly consistent with the expected lensed number counts down to ~ 27 mag, where we begin to suffer significant ($> 50\%$) and dramatically increasing incompleteness. In particular, in all three redshift bins we find a higher number density at brighter observed magnitudes than the field predictions. The observed number counts for our $z \sim 6$ sample, where we have good statistics, are overall in excellent agreement with the lensed expectations down to 27 AB mag. The $z \sim 7$ and $z \sim 8$ samples likely suffer from the effects of small sample statistics, but the lensing effect is still clearly evident at bright magnitudes where the lensing effect is most pronounced because of the steepness of the LF. A more detailed exploration of incompleteness and contamination of our high-redshift candidates will be explored in an upcoming study to derive accurate effective volumes behind the clusters and lensed LFs in a Bayesian framework (L. A. Moustakas et al., in preparation)

8. SUMMARY

We have analyzed the 16 band *HST* observations of 18 lensing clusters obtained as part of the CLASH MCT program to search for $z \sim 6 - 8$ galaxies. Using purely photometric redshift selections, we find 204, 45, and 13 high-redshift LBG candidates at $z \sim 6$, $z \sim 7$, and $z \sim 8$, respectively. Our large sample of magnified star-forming galaxies at these redshifts represents the largest sample presented to date, nearly an order of magnitude larger than previous lensed samples. The accurate photometric redshift selections obtained here are enabled by our observations of these $z \sim 6 - 8$ LBG candidates in seven ACS optical and all five WFC3/IR broadband filters.

We constructed detailed lensing models for 17 of the 18 clusters (excluding RXJ1532) searched in this paper. We utilize these models to both estimate object magnifications and to identify two new multiply lensed $z \gtrsim 6$ candidates. The median magnifications provided by these 17 clusters are 4.2, 4.2, and 4.5 for the $z \sim 6$, $z \sim 7$, and $z \sim 8$ samples, respectively, over an average area of 4.5 arcmin^2 per cluster. We note that the highest magnifications have the largest magnification errors due to inherent uncertainties in the precise location of the critical curves, as discussed in Section 6.2.

The intrinsic magnitudes in the relatively shallow CLASH survey reach deeper (> 29.5 AB mag) than the ultra-deep HUDF12 observations thanks to the strong lensing effect. Our observations of the 17 clusters cover a total area of $\sim 22.9 \text{ arcmin}^2$ with magnifications $\mu > 6.3$, needed to surpass the depth of the HUDF12 observations.

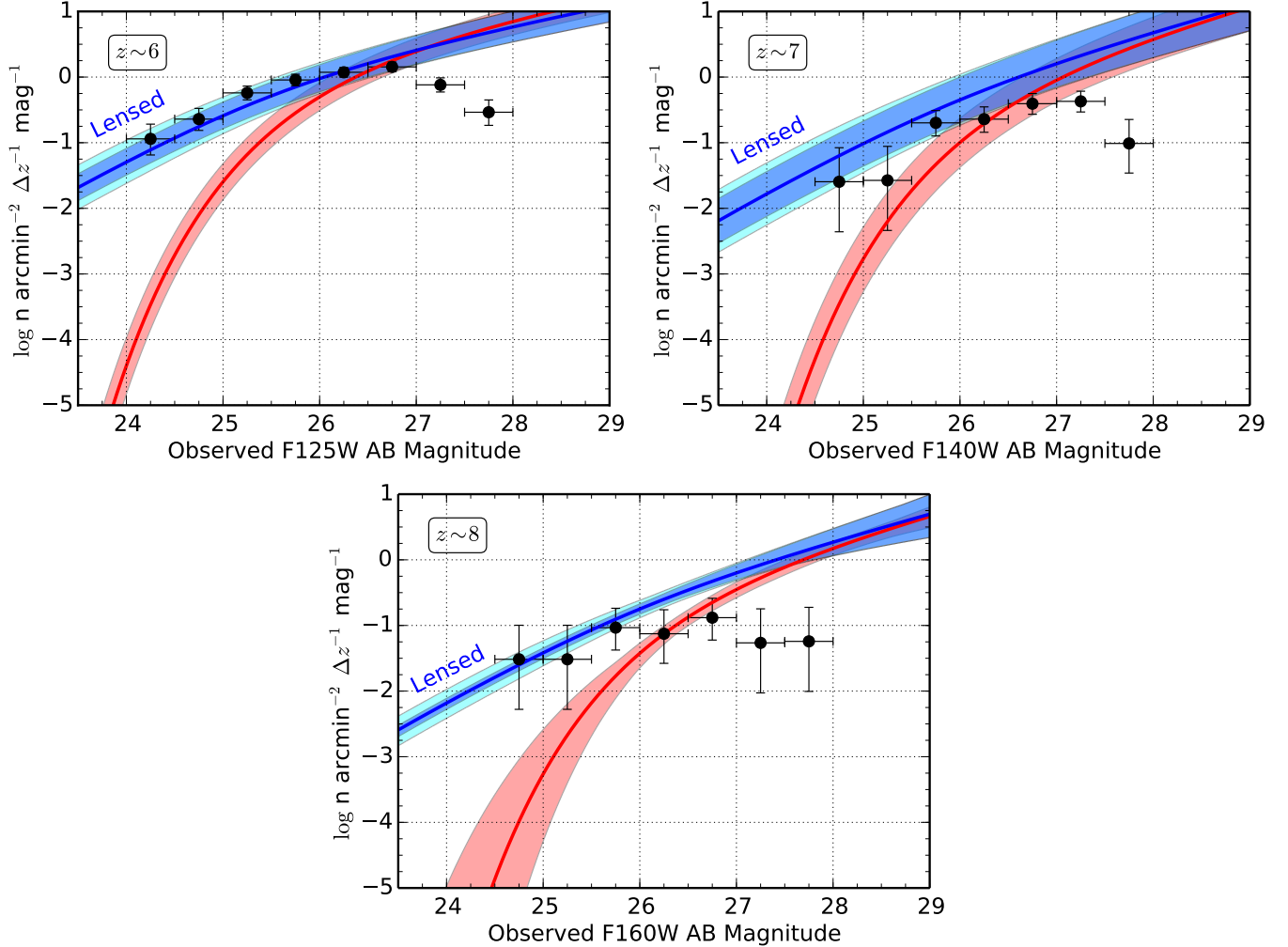


Figure 13. Observed number counts for our lensed galaxy samples at $z \sim 6$ (top left), $z \sim 7$ (top right), and $z \sim 8$ (bottom). The black data points, with 68% (1σ) confidence intervals for a Poisson distribution, represent the number densities over the 17 clusters, covering 76.9 arcmin² in total. The red curves, with shaded 1σ regions, are the expected number densities calculated from “blank” field UV LFs. The $z \sim 6$ and $z \sim 7$ LFs are derived from the UDF09+ERS deep fields (Bouwens et al. 2011), while the $z \sim 8$ LF was derived from a combination of wide and deep BoRG+HUDF09+ERS data (Bradley et al. 2012b). The blue curves are the expected number densities derived by simulating the lensing effect on the field LFs using the cluster lens models. The cyan regions include the additional errors introduced by the uncertainties in the cluster lens models. As can be seen in the figure, the observed number counts of our lensed high-redshift sample are roughly consistent with the expected lensed number counts down to ~ 27 mag, where we begin to suffer significant ($> 50\%$) incompleteness. This is especially true at $z \sim 6$, where we have the best statistics. We also note that our observed number densities are higher than one would expect from a “blank” field survey at the brightest magnitudes, where the lensing effects are most significant because of the steepness of the LF.

This is a relatively robust measure of area in spite of the model uncertainties (see Section 6.3).

Utilizing our detailed lensing models, we identified seven likely multiple image systems over the 17 clusters explored in this paper. Five of them have been previously found in CLASH data: the spectroscopically confirmed $z = 6.027$ system in Abell 383 (Richard et al. 2011), the quadruply lensed galaxy at $z \sim 6.2$ in MACS0329 (Zitrin et al. 2012b), the spectroscopically confirmed quadruple system at $z = 5.701$ in MACS1206 (Zitrin et al. 2012c), a doubly lensed galaxy at $z \sim 6$ in MACS0416 (Zitrin et al. 2013b), and a quintuply lensed $z \sim 5.9$ galaxy in RXCJ2248 (Monna et al. 2014), which have been spectroscopically confirmed at $z = 6.11$ from our CLASH-VLT program (Balestra et al. 2013). We find two new multiply lensed systems, one at $z \sim 6.5$ in MACS0647 and one at $z \sim 6.6$ in MACS0744. In total, this represents

the largest sample of multiply imaged LBGs at $z > 5.5$ presented to date.

Finally, we compare “blank” field UV LFs with their lensed counterparts and our observed number counts with expectations based on convolving “blank” field UV LFs with the 17 cluster lens models. We find that lensing clusters are more efficient than blank field surveys in searching for $z \gtrsim 7$ galaxies down to at least 29 AB mag. This result follows from the apparent increased steepness of the faint-end slope of the UV luminosity function at $z \sim 7 - 8$ with $\alpha \sim -2.0$ (e.g., Bouwens et al. 2011; Oesch et al. 2012; Bradley et al. 2012b; Schenker et al. 2013; McLure et al. 2013). At $z \sim 6$, we find that lensing clusters are more efficient than field surveys at the bright end down to ~ 26 AB mag due to the relatively shallower faint-end slope of $\alpha \sim -1.75$ (Bouwens et al. 2011).

The observed number counts of our lensed high-

redshift sample are approximately consistent with the expected lensed number counts down to ~ 27 mag, where we begin to suffer significant incompleteness. Our number counts have been corrected for a small ($\sim 12\%$) contamination from low-redshift red galaxies (see Section 5.3). Where we have our best statistics at $z \sim 6$, we find our observed number counts overall to be in excellent agreement with the lensed expectations down to 27 AB mag. For the $z \sim 7$ and $z \sim 8$ samples, which likely suffer from the effects of small number statistics, the lensing effect is also clearly evident at bright magnitudes where the lensing effect is most pronounced. In all three redshift bins, our observed number densities are higher than one would expect from a “blank” field survey at the brightest magnitudes, where the lensing effects are most significant because of the steepness of the LF.

This large new sample of lensed star-forming galaxies at $z \gtrsim 5.5$ provides a wealth of information on galaxies in the reionization epoch of the universe. Because these galaxies are brighter than typical field surveys, a sample of high-redshift CLASH candidates have also been detected and studied with *Spitzer*/IRAC at $3.6\mu\text{m}$ and $4.5\mu\text{m}$, elucidating their stellar masses and specific star-formation rates (Zitrin et al. 2012b; Zheng et al. 2012; Coe et al. 2013; Smit et al. 2014) and nebular emission-line strengths (Smit et al. 2014). Future work will focus on additional spectroscopic followup observations, investigating their rest-frame UV colors, deriving accurate effective volumes behind the clusters and lensed UV LFs in a Bayesian framework (L. A. Moustakas et al., in preparation), and studying their intrinsic sizes and morphologies.

With the recent exciting CLASH discoveries of two $z \sim 9$ candidates (Bouwens et al. 2012a), a $z \sim 9.6$ candidate (Zheng et al. 2012), and a triply lensed candidate at $z \sim 10.7$ behind MACS0647 (Coe et al. 2013), lensing clusters have proven to be a powerful tool in the discovery and study of high-redshift galaxies. This technique will continue to be availed with the HFF campaign, which will obtain ultra-deep ACS and WFC3/IR observations of four to six lensing clusters (four of which are presented in this paper) to unprecedented depths.

We thank the anonymous referee for very helpful feedback that improved the paper. We are especially grateful to our program coordinator Beth Perrillo for her expert assistance in implementing the *HST* observations in this program. We thank Jay Anderson and Norman Grogin for providing the ACS CTE and bias striping correction algorithms used in our data pipeline. Finally, we are indebted to the hundreds of people who have labored many years to plan, develop, manufacture, install, repair, and calibrate the WFC3 and ACS instruments as well as to all those who maintain and operate the *Hubble Space Telescope*.

The CLASH Multi-Cycle Treasury Program (GO-12065) is based on observations made with the NASA/ESA Hubble Space Telescope. The Space Telescope Science Institute is operated by the Association of Universities for Research in Astronomy, Inc. under NASA contract NAS 5-26555. A.Z. is supported by contract research “Internationale Spitzenforschung II/2-6” of the Baden Württemberg Stiftung. The work of

L.A.M., J.M., and M.M. was carried out at Jet Propulsion Laboratory, California Institute of Technology, under a contract with NASA. The Dark Cosmology Centre is funded by the DNRF.

REFERENCES

- Arnouts, S., Cristiani, S., Moscardini, L., Matarrese, S., Lucchin, F., Fontana, A., & Giallongo, E. 1999, *MNRAS*, 310, 540 [ADS]
- Atek, H., Siana, B., Scarlata, C., et al. 2011, *ApJ*, 743, 121 [ADS]
- Balestra, I., Vanzella, E., Rosati, P., et al. 2013, *A&A*, 559, L9 [ADS]
- Benítez, N. 2000, *ApJ*, 536, 571 [ADS]
- Benítez, N., Ford, H., Bouwens, R., et al. 2004, *ApJS*, 150, 1 [ADS]
- Bertin, E. & Arnouts, S. 1996, *A&AS*, 117, 393 [ADS]
- Bouwens, R., Bradley, L., Zitrin, A., et al. 2012a, *ArXiv e-prints*, 1211.2230 [ADS]
- Bouwens, R. J., Illingworth, G. D., Blakeslee, J. P., Broadhurst, T. J., & Franx, M. 2004, *ApJ*, 611, L1 [ADS]
- Bouwens, R. J., Illingworth, G. D., Bradley, L. D., et al. 2009, *ApJ*, 690, 1764 [ADS]
- Bouwens, R. J., Illingworth, G. D., Franx, M., & Ford, H. 2007, *ApJ*, 670, 928 [ADS]
- Bouwens, R. J., Illingworth, G. D., Oesch, P. A., et al. 2012b, *ApJ*, 754, 83 [ADS]
- Bouwens, R. J., Illingworth, G. D., Oesch, P. A., et al. 2011, *ApJ*, 737, 90 [ADS]
- Bouwens, R. J., Illingworth, G. D., Oesch, P. A., et al. 2013, *ArXiv e-prints*, 1306.2950 [ADS]
- Bradač, M., Treu, T., Applegate, D., et al. 2009, *ApJ*, 706, 1201 [ADS]
- Bradač, M., Vanzella, E., Hall, N., et al. 2012, *ApJ*, 755, L7 [ADS]
- Bradley, L. D., Bouwens, R. J., Ford, H. C., et al. 2008, *ApJ*, 678, 647 [ADS]
- Bradley, L. D., Bouwens, R. J., Zitrin, A., et al. 2012a, *ApJ*, 747, 3 [ADS]
- Bradley, L. D., Trenti, M., Oesch, P. A., et al. 2012b, *ApJ*, 760, 108 [ADS]
- Broadhurst, T., Benítez, N., Coe, D., et al. 2005, *ApJ*, 621, 53 [ADS]
- Broadhurst, T. J., Taylor, A. N., & Peacock, J. A. 1995, *ApJ*, 438, 49 [ADS]
- Bunker, A. J., Wilkins, S., Ellis, R. S., et al. 2010, *MNRAS*, 409, 855 [ADS]
- Calzetti, D., Armus, L., Bohlin, R. C., Kinney, A. L., Koornneef, J., & Storchi-Bergmann, T. 2000, *ApJ*, 533, 682 [ADS]
- Casertano, S., de Mello, D., Dickinson, M., et al. 2000, *AJ*, 120, 2747 [ADS]
- Cimatti, A., Daddi, E., Mignoli, M., et al. 2002, *A&A*, 381, L68 [ADS]
- Coe, D., Benítez, N., Sánchez, S. F., Jee, M., Bouwens, R., & Ford, H. 2006, *AJ*, 132, 926 [ADS]
- Coe, D., Umetsu, K., Zitrin, A., et al. 2012, *ApJ*, 757, 22 [ADS]
- Coe, D., Zitrin, A., Carrasco, M., et al. 2013, *ApJ*, 762, 32 [ADS]
- Cushing, M. C., Rayner, J. T., & Vacca, W. D. 2005, *ApJ*, 623, 1115 [ADS]
- Dunlop, J. S. 2013, *Astrophysics and Space Science Library*, 396, 223 [ADS]
- Dunlop, J. S., Rogers, A. B., McLure, R. J., et al. 2013, *MNRAS*, 432, 3520 [ADS]
- Ebeling, H., Barrett, E., Donovan, D., Ma, C.-J., Edge, A. C., & van Speybroeck, L. 2007, *ApJ*, 661, L33 [ADS]
- Ebeling, H., Edge, A. C., & Henry, J. P. 2001, *ApJ*, 553, 668 [ADS]
- Ebeling, H., Edge, A. C., Mantz, A., Barrett, E., Henry, J. P., Ma, C. J., & van Speybroeck, L. 2010, *MNRAS*, 407, 83 [ADS]
- Egami, E., Kneib, J.-P., Rieke, G. H., et al. 2005, *ApJ*, 618, L5 [ADS]
- Eichner, T., Seitz, S., Suyu, S. H., et al. 2013, *ApJ*, 774, 124 [ADS]
- Ellis, R. S., McLure, R. J., Dunlop, J. S., et al. 2013, *ApJ*, 763, L7 [ADS]
- Ferguson, H. C., Dickinson, M., Giavalisco, M., et al. 2004, *ApJ*, 600, L107 [ADS]

- Finkelstein, S. L., Papovich, C., Giavalisco, M., Reddy, N. A., Ferguson, H. C., Koekemoer, A. M., & Dickinson, M. 2010, *ApJ*, 719, 1250 [ADS]
- Fioc, M. & Rocca-Volmerange, B. 1997, *A&A*, 326, 950 [ADS]
- Franx, M., Illingworth, G. D., Kelson, D. D., van Dokkum, P. G., & Tran, K.-V. 1997, *ApJ*, 486, L75 [ADS]
- Giallongo, E., Salimbeni, S., Menci, N., Zamorani, G., Fontana, A., Dickinson, M., Cristiani, S., & Pozzetti, L. 2005, *ApJ*, 622, 116 [ADS]
- Grazian, A., Castellano, M., Fontana, A., et al. 2012, *A&A*, 547, A51 [ADS]
- Grogin, N. A., Kocevski, D. D., Faber, S. M., et al. 2011, *ApJS*, 197, 35 [ADS]
- Guo, Y., Ferguson, H. C., Giavalisco, M., et al. 2013, *ApJS*, 207, 24 [ADS]
- Hall, N., Bradač, M., Gonzalez, A. H., et al. 2012, *ApJ*, 745, 155 [ADS]
- Ilbert, O., Arnouts, S., McCracken, H. J., et al. 2006, *A&A*, 457, 841 [ADS]
- Ilbert, O., Capak, P., Salvato, M., et al. 2009, *ApJ*, 690, 1236 [ADS]
- Jouvel, S., Host, O., Lahav, O., et al. 2014, *A&A*, 562, A86 [ADS]
- Kneib, J.-P., Ellis, R. S., Santos, M. R., & Richard, J. 2004, *ApJ*, 607, 697 [ADS]
- Koekemoer, A. M., Faber, S. M., Ferguson, H. C., et al. 2011, *ApJS*, 197, 36 [ADS]
- Koekemoer, A. M., Fruchter, A. S., Hook, R. N., & Hack, W. 2003, in *The 2002 HST Calibration Workshop : Hubble after the Installation of the ACS and the NICMOS Cooling System*, ed. S. Arribas, A. Koekemoer, & B. Whitmore, 337
- Kron, R. G. 1980, *ApJS*, 43, 305 [ADS]
- Labbé, I., González, V., Bouwens, R. J., et al. 2010, *ApJ*, 716, L103 [ADS]
- Labbé, I., Oesch, P. A., Bouwens, R. J., et al. 2013, *ApJ*, 777, L19 [ADS]
- Lorenzoni, S., Bunker, A. J., Wilkins, S. M., Stanway, E. R., Jarvis, M. J., & Caruana, J. 2011, *MNRAS*, 414, 1455 [ADS]
- Madau, P. 1995, *ApJ*, 441, 18 [ADS]
- Maizy, A., Richard, J., de Leo, M. A., Pelló, R., & Kneib, J. P. 2010, *A&A*, 509, A105 [ADS]
- Mann, A. W. & Ebeling, H. 2012, *MNRAS*, 420, 2120 [ADS]
- McLure, R. J., Dunlop, J. S., Bowler, R. A. A., et al. 2013, *MNRAS*, 432, 2696 [ADS]
- McLure, R. J., Dunlop, J. S., Cirasuolo, M., Koekemoer, A. M., Sabbi, E., Stark, D. P., Targett, T. A., & Ellis, R. S. 2010, *MNRAS*, 403, 960 [ADS]
- McLure, R. J., Dunlop, J. S., de Ravel, L., et al. 2011, *MNRAS*, 418, 2074 [ADS]
- Medezinski, E., Umetsu, K., Nonino, M., et al. 2013, *ApJ*, 777, 43 [ADS]
- Meneghetti, M., Melchior, P., Grazian, A., et al. 2008, *A&A*, 482, 403 [ADS]
- Meneghetti, M., Rasia, E., Merten, J., Bellagamba, F., Ettori, S., Mazzotta, P., Dolag, K., & Marri, S. 2010, *A&A*, 514, A93 [ADS]
- Monna, A., Seitz, S., Greisel, N., et al. 2014, *MNRAS*, 438, 1417 [ADS]
- Oesch, P. A., Bouwens, R. J., Carollo, C. M., et al. 2010a, *ApJ*, 709, L21 [ADS]
- Oesch, P. A., Bouwens, R. J., Illingworth, G. D., et al. 2010b, *ApJ*, 709, L16 [ADS]
- Oesch, P. A., Bouwens, R. J., Illingworth, G. D., et al. 2012, *ApJ*, 759, 135 [ADS]
- Oke, J. B. 1974, *ApJS*, 27, 21 [ADS]
- Ono, Y., Ouchi, M., Curtis-Lake, E., et al. 2013, *ApJ*, 777, 155 [ADS]
- Pickles, A. J. 1998, *PASP*, 110, 863 [ADS]
- Postman, M., Coe, D., Benítez, N., et al. 2012, *ApJS*, 199, 25 [ADS]
- Prevot, M. L., Lequeux, J., Prevot, L., Maurice, E., & Rocca-Volmerange, B. 1984, *A&A*, 132, 389 [ADS]
- Rayner, J. T., Cushing, M. C., & Vacca, W. D. 2009, *ApJS*, 185, 289 [ADS]
- Richard, J., Kneib, J.-P., Ebeling, H., Stark, D. P., Egami, E., & Fiedler, A. K. 2011, *MNRAS*, 414, L31 [ADS]
- Richard, J., Stark, D. P., Ellis, R. S., George, M. R., Egami, E., Kneib, J.-P., & Smith, G. P. 2008, *ApJ*, 685, 705 [ADS]
- Saro, A., Borgani, S., Tornatore, L., Dolag, K., Murante, G., Biviano, A., Calura, F., & Charlot, S. 2006, *MNRAS*, 373, 397 [ADS]
- Schenker, M. A., Robertson, B. E., Ellis, R. S., et al. 2013, *ApJ*, 768, 196 [ADS]
- Schenker, M. A., Stark, D. P., Ellis, R. S., Robertson, B. E., Dunlop, J. S., McLure, R. J., Kneib, J.-P., & Richard, J. 2012, *ApJ*, 744, 179 [ADS]
- Schlegel, D. J., Finkbeiner, D. P., & Davis, M. 1998, *ApJ*, 500, 525 [ADS]
- Sharon, K., Gladders, M. D., Rigby, J. R., Wuyts, E., Koester, B. P., Bayliss, M. B., & Barrientos, L. F. 2012, *ApJ*, 746, 161 [ADS]
- Smit, R., Bouwens, R. J., Labbé, I., et al. 2014, *ApJ*, 784, 58 [ADS]
- Steidel, C. C., Giavalisco, M., Dickinson, M., & Adelberger, K. L. 1996, *AJ*, 112, 352 [ADS]
- Swinbank, A. M., Webb, T. M., Richard, J., et al. 2009, *MNRAS*, 400, 1121 [ADS]
- Trenti, M., Bradley, L. D., Stiavelli, M., et al. 2011, *ApJ*, 727, L39 [ADS]
- Trenti, M., Bradley, L. D., Stiavelli, M., et al. 2012a, *ApJ*, 746, 55 [ADS]
- Trenti, M., Perna, R., Levesque, E. M., Shull, J. M., & Stocke, J. T. 2012b, *ApJ*, 749, L38 [ADS]
- van der Wel, A., Straughn, A. N., Rix, H.-W., et al. 2011, *ApJ*, 742, 111 [ADS]
- Vanzella, E., Fontana, A., Zitrin, A., et al. 2014, *ApJ*, 783, L12 [ADS]
- Wilkins, S. M., Bunker, A. J., Stanway, E., Lorenzoni, S., & Caruana, J. 2011, *MNRAS*, 417, 717 [ADS]
- Windhorst, R. A., Cohen, S. H., Hathi, N. P., et al. 2011, *ApJS*, 193, 27 [ADS]
- Wuyts, S., Labbé, I., Schreiber, N. M. F., Franx, M., Rudnick, G., Brammer, G. B., & van Dokkum, P. G. 2008, *ApJ*, 682, 985 [ADS]
- Yan, H., Finkelstein, S. L., Huang, K.-H., et al. 2012, *ApJ*, 761, 177 [ADS]
- Yan, H., Yan, L., Zamojski, M. A., et al. 2011, *ApJ*, 728, L22 [ADS]
- Zheng, W., Bradley, L. D., Bouwens, R. J., et al. 2009, *ApJ*, 697, 1907 [ADS]
- Zheng, W., Postman, M., Zitrin, A., et al. 2012, *Nature*, 489, 406 [ADS]
- Zitrin, A., Broadhurst, T., Bartelmann, M., Rephaeli, Y., Oguri, M., Benítez, N., Hao, J., & Umetsu, K. 2012a, *MNRAS*, 423, 2308 [ADS]
- Zitrin, A., Broadhurst, T., Coe, D., et al. 2011, *ApJ*, 742, 117 [ADS]
- Zitrin, A., Broadhurst, T., Umetsu, K., et al. 2009, *MNRAS*, 396, 1985 [ADS]
- Zitrin, A., Menanteau, F., Hughes, J. P., Coe, D., Barrientos, L. F., Infante, L., & Mandelbaum, R. 2013a, *ApJ*, 770, L15 [ADS]
- Zitrin, A., Meneghetti, M., Umetsu, K., et al. 2013b, *ApJ*, 762, L30 [ADS]
- Zitrin, A., Moustakas, J., Bradley, L., et al. 2012b, *ApJ*, 747, L9 [ADS]
- Zitrin, A., Rosati, P., Nonino, M., et al. 2012c, *ApJ*, 749, 97 [ADS]
- . 2012d, *ApJ*, 749, 97 [ADS]

Table 4 — *Continued*

Object ID	α_{J2000}	δ_{J2000}	I_{814}	z_{850}	Y_{105}	Y_{110}	J_{125}	J_{140}	H_{160}	$z_{\text{phot}}^{\text{a}}$	μ^{b}
-----------	------------------	------------------	-----------	-----------	-----------	-----------	-----------	-----------	-----------	------------------------------	------------------

Note. — Magnitudes are expressed as observed (lensed) isophotal magnitudes (ISOMAG).

^a Photometric redshift estimate with 2σ (95%) confidence intervals (see Section 4). Objects with large lower bounds have a secondary peak at lower redshift ($z \sim 1 - 2$) that contains at least 5% of the posterior probability.

^b Magnification estimate from the lens models (see Section 6). Because of uncertainties in the precise location of the critical curves, objects with magnifications > 100 are simply quoted as such. Objects outside the region constrained by the strong lensing models have been assigned a magnification of 1.1.

^c Unresolved object with FWHM < 0.22 arcsec in the image plane. There is a small chance that brighter unresolved candidates could be low-mass stars even though we explored such possibilities (see Section 5.3).

^d Using LePhare, we find that these unresolved candidates have a good fit with stellar templates, with χ_{star}^2 comparable or less than χ_{galaxy}^2 .

^e While BPZ prefers a high-redshift solution, we note that LePhare slightly prefers a low-redshift solution ($z \sim 1$) over the high-redshift solution for these three galaxies. Given this and the possible fit with stellar templates, these candidates should be considered less confident than the others.

^f Spectroscopically confirmed multiply-imaged galaxy at $z = 6.027$ (Richard et al. 2011).

^g Quadruply lensed galaxy at $z \sim 6.2$ (Zitrin et al. 2012b).

^h Zitrin et al. (2013b) report that MACS0419-0419 is part of a visually identified double system at $z_{\text{phot}} \sim 6.1$. The second candidate (at R.A. = 04:16:09.946, Dec = -24:03:45.31) fell below our S/N threshold and thus does not appear in this catalog.

ⁱ MACS1115-0352 and MACS1720-1114 have very blue SEDs. While our best-fit photometric redshifts suggest that these are high-redshift candidates, a possible alternative solution is that they could be low-redshift extreme emission-line galaxies with rest-frame equivalent widths of ~ 2000 Å (X. Huang et al. 2014, submitted).

^j Quadruply lensed galaxy at $z_{\text{phot}} \sim 5.6$ ($z_{\text{spec}} = 5.701$) (Zitrin et al. 2012d).

^k VLT/VIMOS spectroscopy confirms this galaxy at $z = 5.701$ (see Section 5).

^l Monna et al. (2014) found that these two candidates, along with three others, are part of a quintuply-lensed system with $z_{\text{phot}} \sim 5.9$. Based on their lens model, the magnifications for RXCJ2248-0401 and RXCJ2248-1291 (ID4 and ID3, respectively in Monna et al. (2014)) are 2.4 ± 0.2 and 6.0 ± 1.5 , respectively.

^m In the recent Hubble Frontier Fields data, this candidate is detected in the ultra-deep optical data and therefore it is very unlikely to be a high-redshift galaxy.

ⁿ MACS0717-0859 and MACS0717-1730 are spectroscopically confirmed at $z = 6.387$ (Vanzella et al. 2014).

Table 6
Lensed $z \sim 8$ Candidates Identified Behind 17 CLASH Clusters

Object ID	α_{J2000}	δ_{J2000}	I_{814}	z_{850}	Y_{105}	Y_{110}	J_{125}	J_{140}	H_{160}	$z_{\text{phot}}^{\text{a}}$	μ^{b}
A2261-0187	260.6073833	32.1495175	> 29.3	> 28.4	27.4 ± 0.19	27.3 ± 0.13	26.8 ± 0.13	26.8 ± 0.11	27.0 ± 0.13	$7.5^{+0.4}_{-1.2}$	2.9
A383-2311	42.0149347	-3.5526143	> 29.3	28.0 ± 0.60	27.7 ± 0.35	...	26.9 ± 0.15	26.7 ± 0.16	27.2 ± 0.23	$7.5^{+0.9}_{-6.4}$	4.5
A611-0193	120.2513506	36.0734262	28.5 ± 0.54	28.1 ± 0.74	27.0 ± 0.19	...	26.0 ± 0.09	26.0 ± 0.10	26.0 ± 0.17	$7.9^{+0.3}_{-6.5}$	1.6
MACS0416-1830 ^c	64.0379772	-24.0888285	> 29.1	> 28.7	29.0 ± 0.58	28.6 ± 0.32	28.0 ± 0.25	27.8 ± 0.19	28.2 ± 0.26	$8.1^{+0.7}_{-7.7}$	1.6
MACS0647-1411	101.9204414	70.2448881	28.9 ± 0.58	> 27.9	26.7 ± 0.18	26.6 ± 0.11	26.1 ± 0.10	26.0 ± 0.08	26.1 ± 0.08	$7.6^{+0.5}_{-6.3}$	> 100
MACS1115-0356	168.962901	1.5097067	28.4 ± 0.62	> 27.9	27.2 ± 0.25	27.0 ± 0.18	26.3 ± 0.13	26.1 ± 0.10	26.1 ± 0.10	$8.0^{+0.4}_{-6.7}$	12.0
MACS1206-1581	181.5512693	-8.8084446	> 29.4	> 28.7	28.8 ± 0.53	28.6 ± 0.31	27.8 ± 0.24	28.0 ± 0.24	27.8 ± 0.20	$7.9^{+0.8}_{-7.0}$	4.7
MACS1720-0696 ^{d,e}	260.0466407	35.6144436	> 28.2	> 27.9	26.5 ± 0.15	25.9 ± 0.05	...	25.6 ± 0.07	25.8 ± 0.09	$7.7^{+0.2}_{-1.0}$	1.3
MACS1720-1231	260.0530519	35.6047895	> 29.6	> 28.7	29.1 ± 0.58	28.3 ± 0.23	27.9 ± 0.24	27.6 ± 0.16	27.7 ± 0.19	$8.3^{+0.6}_{-7.1}$	1.7
MACS1931-1990	292.9578406	-26.5913165	> 28.0	> 27.2	25.9 ± 0.11	26.0 ± 0.09	25.5 ± 0.08	25.4 ± 0.07	25.5 ± 0.07	$7.5^{+0.3}_{-0.9}$	27.8
RXJ1347-0943	206.8912473	-11.7526045	> 29.1	> 28.1	27.3 ± 0.31	26.6 ± 0.08	26.4 ± 0.14	26.4 ± 0.12	26.5 ± 0.10	$7.5^{+0.5}_{-1.0}$	> 100
RXCJ2248-1301	342.208379	-44.5375171	> 28.7	> 28.0	27.4 ± 0.32	27.1 ± 0.13	...	26.5 ± 0.14	26.4 ± 0.13	$7.7^{+0.6}_{-6.5}$	1.4

Note. — Magnitudes are expressed as observed (lensed) isophotal magnitudes (ISOMAG).

^a Photometric redshift estimate with 2σ (95%) confidence intervals (see Section 4). Objects with large lower bounds have a secondary peak at lower redshift ($z \sim 1-2$) that contains at least 5% of the posterior probability.

^b Magnification estimate from the lens models (see Section 6). Because of uncertainties in the precise location of the critical curves, objects with magnifications > 100 are simply quoted as such.

^c In the recent Hubble Frontier Fields data, this candidate is detected in the ultra-deep optical data and therefore it is very unlikely to be a high-redshift galaxy.

^d Unresolved object with FWHM < 0.22 arcsec in the image plane. There is a small chance that brighter unresolved candidates could be low-mass stars even though we explored such possibilities (see Section 5.3).

^e Using LePhare, we find that this unresolved candidate has a good fit with stellar templates, with χ_{star}^2 comparable or less than χ_{galaxy}^2 .

A. HIGH-REDSHIFT CANDIDATES BEHIND RXJ1532.9+3021

In Table 7, we list the high-redshifts candidates identified behind RXJ1532.9+3021. For this cluster, we have not been able to clearly identify any multiply imaged galaxies that are required to constrain the strong lensing model. However, we have generated an approximate model of this cluster constrained based solely on the light distribution (e.g., Zitrin et al. 2012a), without any information of multiple images as constraints. Such models, utilizing the useful parameterizations of this modeling method, were found to be accurate at the level of $\sim 20\%$ on the mass and location of the critical curves, but magnification errors can be higher (Zitrin et al. 2012a). Using this model, we include our magnification estimates for these candidates, but the important caveats about this lens model need to be taken into consideration.

Table 7
Lensed Candidates Identified Behind RXJ1532.9+3021

Object ID	α_{J2000}	δ_{J2000}	I_{814}	z_{850}	Y_{105}	Y_{110}	J_{125}	J_{140}	H_{160}	$z_{\text{phot}}^{\text{a}}$	μ^{b}
RXJ1532-0080	233.2324699	30.3692524	28.7 ± 0.54	26.9 ± 0.30	26.5 ± 0.17	...	26.6 ± 0.13	26.5 ± 0.13	26.6 ± 0.17	$6.3^{+0.4}_{-5.3}$	5.0
RXJ1532-0324	233.2474354	30.3620154	26.7 ± 0.19	26.3 ± 0.28	26.0 ± 0.16	25.3 ± 0.05	...	25.9 ± 0.17	25.7 ± 0.13	$6.2^{+0.2}_{-5.9}$	2.5
RXJ1532-0390	233.2245355	30.3604005	> 28.6	28.2 ± 0.73	27.5 ± 0.25	27.1 ± 0.13	27.6 ± 0.28	27.4 ± 0.19	27.6 ± 0.24	$6.3^{+0.8}_{-5.5}$	4.0
RXJ1532-0471	233.2370996	30.3589943	28.1 ± 0.34	> 27.7	26.8 ± 0.15	27.1 ± 0.15	26.7 ± 0.15	26.9 ± 0.15	26.8 ± 0.14	$6.1^{+0.8}_{-5.7}$	4.5
RXJ1532-0488	233.2463449	30.358271	27.5 ± 0.17	26.8 ± 0.19	26.9 ± 0.17	27.3 ± 0.14	...	26.9 ± 0.14	27.4 ± 0.24	$5.5^{+0.3}_{-0.7}$	3.8
RXJ1532-0594	233.2336512	30.3554857	28.5 ± 0.43	26.9 ± 0.22	26.9 ± 0.14	27.0 ± 0.11	27.7 ± 0.27	27.8 ± 0.26	27.3 ± 0.17	$5.9^{+0.4}_{-0.3}$	4.3
RXJ1532-0682	233.2312664	30.3542801	27.4 ± 0.29	26.7 ± 0.34	26.2 ± 0.12	26.5 ± 0.12	26.7 ± 0.19	26.6 ± 0.15	26.6 ± 0.15	$6.0^{+0.4}_{-0.6}$	14.7
RXJ1532-0683	233.2141861	30.3545029	> 29.0	28.3 ± 0.71	27.3 ± 0.19	27.4 ± 0.15	27.1 ± 0.17	27.9 ± 0.26	27.4 ± 0.19	$6.4^{+0.6}_{-6.2}$	6.6
RXJ1532-0712	233.2502805	30.3527546	27.7 ± 0.24	26.8 ± 0.24	26.5 ± 0.17	...	27.2 ± 0.19	26.9 ± 0.16	26.7 ± 0.16	$5.6^{+0.5}_{-5.2}$	3.8
RXJ1532-0716	233.2312519	30.3529432	> 28.6	26.3 ± 0.20	27.1 ± 0.22	26.7 ± 0.11	27.0 ± 0.20	27.3 ± 0.22	26.8 ± 0.16	$5.7^{+0.5}_{-5.7}$	> 100
RXJ1532-0771	233.2130381	30.3519917	29.2 ± 0.70	27.0 ± 0.26	27.2 ± 0.18	27.5 ± 0.16	27.6 ± 0.23	27.4 ± 0.17	27.5 ± 0.20	$5.8^{+0.6}_{-5.3}$	4.3
RXJ1532-0916	233.2457329	30.3488797	28.8 ± 0.66	27.2 ± 0.37	25.8 ± 0.12	...	26.6 ± 0.15	26.8 ± 0.20	26.7 ± 0.19	$6.4^{+0.3}_{-0.3}$	5.1
RXJ1532-1100	233.2138441	30.3442524	27.8 ± 0.32	27.1 ± 0.36	26.5 ± 0.13	26.6 ± 0.10	26.8 ± 0.18	26.4 ± 0.11	26.6 ± 0.13	$5.7^{+0.7}_{-5.7}$	3.5
RXJ1532-1127	233.2263652	30.344196	27.5 ± 0.20	26.2 ± 0.16	26.7 ± 0.13	26.8 ± 0.11	26.9 ± 0.15	26.9 ± 0.13	27.3 ± 0.18	$5.6^{+0.2}_{-4.7}$	15.6
RXJ1532-1241	233.2192718	30.3407408	28.8 ± 0.59	26.7 ± 0.22	26.8 ± 0.15	26.8 ± 0.11	26.9 ± 0.16	26.7 ± 0.12	27.0 ± 0.16	$6.1^{+0.4}_{-0.5}$	5.4
RXJ1532-1538 ^c	233.2227919	30.3306261	27.9 ± 0.32	26.7 ± 0.25	25.9 ± 0.09	26.0 ± 0.07	25.7 ± 0.07	26.0 ± 0.08	26.0 ± 0.08	$6.3^{+0.4}_{-0.5}$	1.5
RXJ1532-0844	233.2450679	30.3506265	> 28.8	> 27.3	26.5 ± 0.17	25.9 ± 0.07	26.0 ± 0.10	26.1 ± 0.09	26.0 ± 0.09	$7.1^{+0.3}_{-0.8}$	3.4
RXJ1532-0878	233.2152996	30.3530354	28.9 ± 0.65	> 28.2	27.2 ± 0.20	26.7 ± 0.10	27.2 ± 0.20	26.9 ± 0.14	27.1 ± 0.16	$6.5^{+0.7}_{-0.6}$	14.7
RXJ1532-0918	233.2150798	30.3529243	> 28.9	> 28.0	26.2 ± 0.11	26.5 ± 0.10	26.5 ± 0.14	26.8 ± 0.16	26.7 ± 0.14	$6.6^{+0.4}_{-0.2}$	12.8
RXJ1532-1063	233.199579	30.3455558	27.9 ± 0.48	> 27.2	25.7 ± 0.13	...	25.7 ± 0.09	25.6 ± 0.09	25.4 ± 0.09	$6.5^{+0.6}_{-5.4}$	1.0
RXJ1532-0030	233.2273252	30.3721732	> 28.7	> 28.1	27.3 ± 0.30	...	26.4 ± 0.11	26.8 ± 0.16	27.1 ± 0.25	$7.7^{+0.5}_{-1.6}$	4.9

Note. — Magnitudes are expressed as observed (lensed) isophotal magnitudes (ISOMAG).

^a Photometric redshift estimate with 2σ (95%) confidence intervals (see Section 4). Objects with large lower bounds have a secondary peak at lower redshift ($z \sim 1 - 2$) that contains at least 5% of the posterior probability.

^b Magnification estimate from the lens models (see Section 6). Because of uncertainties in the precise location of the critical curves, objects with magnifications > 100 are simply quoted as such.

^c Unresolved object with FWHM < 0.22 arcsec in the image plane. There is a small chance that brighter unresolved candidates could be low-mass stars even though we explored such possibilities (see Section 5.3).